



THE DATA REDUCTION PIPELINE FOR THE SDSS-IV MaNGA IFU GALAXY SURVEY

DAVID R. LAW¹, BRIAN CHERINKA², RENBIN YAN³, BRETT H. ANDREWS⁴, MATTHEW A. BERSHADY⁵, DMITRY BIZYAEV⁶,
 GUILLERMO A. BLANC^{7,8,9}, MICHAEL R. BLANTON¹⁰, ADAM S. BOLTON¹¹, JOEL R. BROWNSTEIN¹¹, KEVIN BUNDY¹²,
 YANMEI CHEN^{13,14}, NIV DRORY¹⁵, RICHARD D'SOUZA¹⁶, HAI FU¹⁷, AMY JONES¹⁶, GUINEVERE KAUFFMANN¹⁶,
 NICHOLAS MACDONALD¹⁸, KAREN L. MASTERS¹⁹, JEFFREY A. NEWMAN⁴, JOHN K. PAREJKO¹⁸, JOSÉ R. SÁNCHEZ-GALLEGO³,
 SEBASTIAN F. SÁNCHEZ²⁰, DAVID J. SCHLEGEL²¹, DANIEL THOMAS¹⁹, DAVID A. WAKE^{5,22}, ANNE-MARIE WEIJMANS²³,
 KYLE B. WESTFALL¹⁹, AND KAI ZHANG³

¹ Space Telescope Science Institute, 3700 San Martin Drive, Baltimore, MD 21218, USA; dlaw@stsci.edu

² Center for Astrophysical Sciences, Department of Physics and Astronomy, Johns Hopkins University, Baltimore, MD 21218, USA

³ Department of Physics and Astronomy, University of Kentucky, 505 Rose Street, Lexington, KY 40506-0055, USA

⁴ Department of Physics and Astronomy and PITT PACC, University of Pittsburgh, 3941 O'Hara Street, Pittsburgh, PA 15260, USA

⁵ Department of Astronomy, University of Wisconsin-Madison, 475 N. Charter Street, Madison, WI 53706, USA

⁶ Apache Point Observatory, P.O. Box 59, Sunspot, NM 88349, USA

⁷ Departamento de Astronomía, Universidad de Chile, Camino del Observatorio 1515, Las Condes, Santiago, Chile

⁸ Centro de Astrofísica y Tecnologías Afines (CATA), Camino del Observatorio 1515, Las Condes, Santiago, Chile

⁹ Visiting Astronomer, Observatories of the Carnegie Institution for Science, 813 Santa Barbara Street, Pasadena, CA, 91101, USA

¹⁰ Center for Cosmology and Particle Physics, Department of Physics, New York University, 4 Washington Place, New York, NY 10003, USA

¹¹ Department of Physics and Astronomy, University of Utah, 115 S 1400 E, Salt Lake City, UT 84112, USA

¹² Kavli Institute for the Physics and Mathematics of the universe, Todai Institutes for Advanced Study, the University of Tokyo, Kashiwa, 277-8583 (Kavli IPMU, WPI), Japan

¹³ School of Astronomy and Space Science, Nanjing University, Nanjing 210093, China

¹⁴ Key Laboratory of Modern Astronomy and Astrophysics (Nanjing University), Ministry of Education, Nanjing 210093, China

¹⁵ McDonald Observatory, Department of Astronomy, University of Texas at Austin, 1 University Station, Austin, TX 78712-0259, USA

¹⁶ Max Planck Institute for Astrophysics, Karl-Schwarzschild-Str. 1, D-85748 Garching, Germany

¹⁷ Department of Physics & Astronomy, University of Iowa, Iowa City, IA 52242, USA

¹⁸ Department of Astronomy, Box 351580, University of Washington, Seattle, WA 98195, USA

¹⁹ Institute of Cosmology and Gravitation, University of Portsmouth, Portsmouth, UK

²⁰ Instituto de Astronomía, Universidad Nacional Autónoma de México, A.P. 70-264, 04510 México D.F., México

²¹ Physics Division, Lawrence Berkeley National Laboratory, Berkeley, CA 94720-8160, USA

²² Department of Physical Sciences, The Open University, Milton Keynes, UK

²³ School of Physics and Astronomy, University of St. Andrews, North Haugh, St. Andrews KY16 9SS, UK

Received 2016 April 5; revised 2016 May 27; accepted 2016 June 9; published 2016 September 12

ABSTRACT

Mapping Nearby Galaxies at Apache Point Observatory (MaNGA) is an optical fiber-bundle integral-field unit (IFU) spectroscopic survey that is one of three core programs in the fourth-generation Sloan Digital Sky Survey (SDSS-IV). With a spectral coverage of 3622–10354 Å and an average footprint of ~ 500 arcsec² per IFU the scientific data products derived from MaNGA will permit exploration of the internal structure of a statistically large sample of 10,000 low-redshift galaxies in unprecedented detail. Comprising 174 individually pluggable science and calibration IFUs with a near-constant data stream, MaNGA is expected to obtain ~ 100 million raw-frame spectra and ~ 10 million reduced galaxy spectra over the six-year lifetime of the survey. In this contribution, we describe the MaNGA Data Reduction Pipeline algorithms and centralized metadata framework that produce sky-subtracted spectrophotometrically calibrated spectra and rectified three-dimensional data cubes that combine individual dithered observations. For the 1390 galaxy data cubes released in Summer 2016 as part of SDSS-IV Data Release 13, we demonstrate that the MaNGA data have nearly Poisson-limited sky subtraction shortward of ~ 8500 Å and reach a typical 10σ limiting continuum surface brightness $\mu = 23.5$ AB arcsec⁻² in a five-arcsecond-diameter aperture in the *g*-band. The wavelength calibration of the MaNGA data is accurate to 5 km s⁻¹ rms, with a median spatial resolution of 2.54 arcsec FWHM (1.8 kpc at the median redshift of 0.037) and a median spectral resolution of $\sigma = 72$ km s⁻¹.

Key words: methods: data analysis – surveys – techniques: imaging spectroscopy

1. INTRODUCTION

Over the last 20 yr, multiplexed spectroscopic surveys have been valuable tools for bringing the power of statistics to bear on the study of galaxy formation. Using large samples of tens to hundreds of thousands of galaxies with optical spectroscopy from the Sloan Digital Sky Survey (York et al. 2000; Abazajian et al. 2003), for instance, studies have outlined fundamental relations between stellar mass, metallicity, element abundance ratios, and star formation history (e.g., Kauffmann et al. 2003; Tremonti et al. 2004; Thomas et al. 2010). However, this

statistical power has historically come at the cost of treating galaxies as point sources, with only a small and biased region subtended by a given optical fiber contributing to the recorded spectrum.

As technology has advanced, techniques have been developed for *imaging spectroscopy* that allow simultaneous spatial and spectral coverage, with correspondingly greater information density for each individual galaxy. Building on early work by (e.g.) Colina et al. (1999) and de Zeeuw et al. (2002), such integral-field spectroscopy has provided a wealth of information. In the nearby universe, for instance, observations from the

DiskMass survey (Bershady et al. 2010) have indicated that late-type galaxies tend to have sub-maximal disks (Bershady et al. 2011), while Atlas-3D observations (Cappellari et al. 2011a) showed that early-type galaxies frequently have rapidly rotating components (especially in low-density environments; Cappellari et al. 2011b). In the more distant universe, integral-field spectroscopic observations have been crucial in establishing the prevalence of high gas-phase velocity dispersions (e.g., Förster Schreiber et al. 2009; Law et al. 2009, 2012; Wisnioski et al. 2015), giant kiloparsec-sized clumps of young stars (e.g., Förster Schreiber et al. 2011), and powerful nuclear outflows (Förster Schreiber et al. 2014) that may indicate fundamental differences in gas accretion mechanisms in the young universe (e.g., Dekel et al. 2009).

More recently, surveys such as the Calar Alto Legacy Integral Field Area Survey (CALIFA, Sánchez et al. 2012; García-Benito et al. 2015), Sydney-AAO Multi-object IFS (SAMI, Croom et al. 2012; Allen et al. 2015) and Mapping Nearby Galaxies at Apache Point Observatory (MaNGA, Bundy et al. 2015) have begun to combine the information density of integral-field spectroscopy with the statistical power of large multiplexed samples. As a part of the fourth generation of the Sloan Digital Sky Survey (SDSS-IV), the MaNGA project bundles single fibers from the Baryon Oscillation Spectroscopic Survey (BOSS) spectrograph (Smee et al. 2013) into integral-field units (IFUs); over the six-year lifetime of the survey (2014–2020) MaNGA will obtain spatially resolved optical+NIR spectroscopy of 10,000 galaxies at redshifts $z \sim 0.02$ – 0.1 . In addition to providing insight into the resolved structure of stellar populations, galactic winds, and dynamical evolution in the local universe (e.g., Belfiore et al. 2015; Li et al. 2015; Wilkinson et al. 2015), the MaNGA data set will be an invaluable legacy product with which to help understand galaxies in the distant universe. As next-generation facilities come online in the final years of the MaNGA survey, IFU spectrographs such as TMT/IRIS (Moore et al. 2014; Wright et al. 2014), *James Webb Space Telescope* (JWST)/NIRSPEC (Closs et al. 2008; Birkmann et al. 2014), and JWST/MIRI-MRS (Wells et al. 2015) will trace the crucial rest-optical bandpass in galaxies out to redshift $z \sim 10$ and beyond.

Imaging spectroscopic surveys such as MaNGA face substantial calibration challenges in order to meet the science requirements of the survey (R. Yan et al. 2016b). In addition to requiring accurate absolute spectrophotometry from each fiber, MaNGA must correct for gravitationally induced flexure variability in the Cassegrain-mounted BOSS spectrographs, determine accurate micron-precision astrometry for each IFU bundle, and combine spectra from the individual fibers with accurate astrometric information in order to construct three-dimensional (3D) data cubes that rectify the wavelength-dependent differential atmospheric refraction (DAR) and (despite large interstitial gaps in the fiber bundles) consistently deliver high-quality *imaging* products. These combined requirements have driven a substantial software pipeline development effort throughout the early years of SDSS-IV.

Historically, IFU data have been processed with a mixture of software tools ranging from custom built pipelines (e.g., Zanichelli et al. 2005) to general-purpose tools capable of performing all or part of the basic data reduction tasks for multiple IFUs. For fiber-fed IFUs (with or without coupled lenslet arrays) that deliver a pseudo-slit of discrete apertures, the raw data are similar in format to traditional multi-object

spectroscopy and have hence been able to build upon an existing code base. In contrast, slicer-based IFUs produce data in a format more akin to long-slit spectroscopy, while pure-lenslet IFUs are different altogether with individual spectra staggered across the detector.

Following Sandin et al. (2010), we provide here a brief overview of some of the common tools for the reduction of data from optical and near-IR IFUs (see also Bershady 2009), including both fiber-fed IFUs with data formats similar to MaNGA and lenslet- and slicer-based IFUs by way of comparison. As shown in Table 1, the IRAF environment remains a common framework for the reduction of data from many facilities, especially Gemini, WIYN, and William Herschel Telescope (WHT). Similarly, the various IFUs at the Very Large Telescope (VLT) can all be reduced with software from a common *ISO* C-based pipeline library, although some other packages (e.g., GIRBLDRS, Blecha et al. 2000) are also capable of reducing data from some VLT IFUs. Substantial effort has been invested in the P3D (Sandin et al. 2010) and R3D (Sánchez 2006) packages as well, which together are capable of reducing data from a wide variety of fiber-fed instruments (including PPAK/LARR, VIRUS-P, SPIRAL, GMOS, VIMOS, *INTEGRAL*, and SparsePak) for which similar extraction and calibration algorithms are generally possible. For survey-style operations, the SAMI survey has adopted a two-stage approach, combining a general-purpose spectroscopic pipeline 2DFDR (Hopkins et al. 2013) with a custom 3D stage to assemble IFU data cubes from individual fiber spectra (Sharp et al. 2015).

Similarly, the MaNGA Data Reduction Pipeline (MANGADRP; hereafter the DRP) is also divided into two components. Like the KUNGFU package (Bolton & Burles 2007), the two-dimensional (2D) stage of the DRP is based largely on the SDSS BOSS spectroscopic reduction pipeline IDLSPEC2D (D. Schlegel et al. 2016, in preparation), and processes the raw CCD data to produce sky-subtracted, flux-calibrated spectra for each fiber. The 3D stage of the DRP is custom built for MaNGA, but adapts core algorithms from the CALIFA (Sánchez et al. 2012) and VENGA (Blanc et al. 2013) pipelines in order to produce astrometrically registered composite data cubes. In the present contribution, we describe version v1_5_4 of the MaNGA DRP corresponding to the first public release of science data products in SDSS Data Release 13 (DR13).²⁴

We start by providing a brief overview of the MaNGA hardware and operational strategy in Section 2, and give an overview of the DRP and related systems in Section 3. We then discuss the individual elements of the DRP in detail, starting with the basic spectral extraction technique (including detector pre-processing, fiber tracing, flat-field, and wavelength calibration) in Section 4. In Section 5 we discuss our method of subtracting the sky background (including the bright atmospheric OH features) from the science spectra, and demonstrate that we achieve nearly Poisson-limited performance shortward of 8500 Å. In Section 6 we discuss the method for spectrophotometric calibration of the MaNGA spectra, and in Section 7 our approach to resampling and combining all of the individual spectra onto a common wavelength solution. We describe the astrometric calibration in Section 8, combining a basic approach that takes into account fiber bundle metrology,

²⁴ DR13 is available at <http://www.sdss.org/dr13/>.

Table 1
IFU Data Reduction Software

Telescope	Spectrograph	IFU	Pipeline	Reference
Fiber-fed IFUs				
AAT Calar Alto 3.5 m	AAOMEGA PMAS	SAMI PPAK	2DFDR P3D R3D IRAF	Sharp et al. (2015) Sandin et al. (2010) Sánchez (2006) ^a Martinsson et al. (2013) ^b
HET McDonald 2.7 m	VIRUS VIRUS-P	VIRUS VIRUS-P	CURE VACCINE VENGA	Snigula et al. (2014) Adams et al. (2011) Blanc et al. (2013)
SDSS 2.5 m	BOSS	MaNGA	MANGADRP	This paper
WHT	WYFFOS	<i>INTEGRAL</i>	IRAF	
WIYN	WIYN Bench Spec.	DensePak SparsePak	IRAF IRAF	Andersen et al. (2006)
Fiber + Lenslet-based IFUs				
AAT Calar Alto 3.5 m	AAOMEGA PMAS	SPIRAL LARR	2DFDR As PPAK above	Hopkins et al. (2013)
Gemini <i>Magellan</i>	GMOS IMACS	GMOS IMACS	IRAF KUNGFU	Bolton & Burles (2007)
VLT	GIRAFFE VIMOS	ARGUS VIMOS	GIRBLDRS ESO CPL ^c VIPGI ESO CPL ^c	Blecha et al. (2000) Zanichelli et al. (2005)
Lenslet-based IFUs				
Keck UH 2.2 m	OSIRIS SNIFS	OSIRIS SNIFS	OSIRISDRP SNURP	Krabbe et al. (2004)
WHT	OASIS SAURON	OASIS SAURON	XOASIS XSAURON	Bacon et al. (2001)
Slicer-based IFUs				
ANU Gemini	WiFeS GNIRS	WiFeS GNIRS	IRAF IRAF	Dopita et al. (2010)
VLT	NIFS KMOS MUSE SINFONI	NIFS KMOS MUSE SINFONI	IRAF ESO CPL ^c , SPARK ESO CPL ^c ESO CPL ^c	Davies et al. (2013) Weilbacher et al. (2012) Modigliani et al. (2007)

Notes.

^a See Sánchez et al. (2012) for details of the implementation for the CALIFA survey.

^b Reference corresponds to the DiskMass survey.

^c See <http://www.eso.org/sci/software/cpl/>.

DAR, and other factors (Section 8.1), and an “extended” astrometry module that registers the MaNGA spectra against SDSS-I broadband imaging (Section 8.2). Using this astrometric information we combine together individual fiber spectra into composite 3D data cubes in Section 9. Finally, we assess the quality of the MaNGA DR13 data products in Section 10, focusing on the effective angular and spectral resolution, wavelength calibration accuracy, and typical depth of the MaNGA spectra compared to other extant surveys. We summarize our conclusions in Section 11. Additionally, we provide an Appendix B in which we outline the structure of the MaNGA DR13 data products and quality-assessment bitmasks.

2. MANGA HARDWARE AND OPERATIONS

2.1. Hardware

The MaNGA hardware design is described in detail by Drory et al. (2015); here we provide a brief summary of the major elements that most closely pertain to the DRP. MaNGA uses

the BOSS optical fiber spectrographs (Smee et al. 2013) installed on the Sloan Digital Sky Survey 2.5 m telescope (Gunn et al. 2006) at Apache Point Observatory (APO) in New Mexico. These two spectrographs interface with a removable cartridge and plugplate system; each of the six MaNGA cartridges contains a full complement of 1423 fibers that can be plugged into holes in pre-drilled plug plates ~ 0.7 m (3°) in diameter and which feed pseudo-slits that align with the spectrograph entrance slits when a given cartridge is mounted on the telescope.

These 1423 fibers are bundled into IFUs ferrules with varying sizes; each cartridge has 12 seven-fiber IFUs that are used for spectrophotometric calibration and 17 science IFUs of sizes varying from 19 to 127 fibers (see Table 2). As detailed by D. Wake et al. (in preparation), this assortment of sizes is chosen to best correspond to the angular diameter distribution of the MaNGA target galaxy sample. The orientation of each IFU on the sky is fixed by use of a locator pin and pinhole a short distance west of the IFU. Additionally, each IFU ferrule

Table 2
MaNGA IFU Complement Per Cartridge

IFU size (fibers)	Purpose	Number of IFUs	N_{sky}^a	Diameter ^b (arcsec)
7	Calibration	12	1	7.5
19	Science	2	2	12.5
37	Science	4	2	17.5
61	Science	4	4	22.5
91	Science	2	6	27.5
127	Science	5	8	32.5

Notes.

^a Number of associated sky fibers per IFU ferrule.

^b Total outer-diameter IFU footprint.

has a complement of associated sky fibers (see Table 2) amounting to a total of 92 individually pluggable sky fibers.

Each fiber is $150\ \mu\text{m}$ in diameter, consisting of a $120\ \mu\text{m}$ glass core surrounded by a doped cladding and protective buffer. The $120\ \mu\text{m}$ core diameter subtends $1.98\ \text{arcsec}$ on the sky at the typical plate scale of $\sim 217.7\ \text{mm degree}^{-1}$. These fibers are terminated into 44 V-groove blocks with 21–39 fibers each that are mounted on the two pseudo-slits. As illustrated in Figure 1, the sky fibers associated with each IFU are located at the ends of each block to minimize crosstalk from adjacent science fibers. In total, spectrograph 1 (2) is fed by 709 (714) individual fibers.

Within each spectrograph a dichroic beamsplitter reflects light blueward of $6000\ \text{\AA}$ into a blue-sensitive camera with a $520\ \text{l/mm}$ grism and transmits red light into a camera with a $400\ \text{l/mm}$ grism (both grisms consist of a VPH transmission grating between two prisms). There are therefore four “frames” worth of data taken for each MaNGA exposure, one each from the cameras b1/b2 (blue cameras on spectrograph 1/2) and r1/r2 (red cameras on spectrograph 1/2). The blue cameras use blue-sensitive $4\text{K} \times 4\text{K}$ e2V CCDs while the red cameras use $4\text{K} \times 4\text{K}$ fully depleted LBNL CCDs, all with $15\ \mu\text{m}$ pixels (Smee et al. 2013). The combined wavelength coverage of the blue and red cameras is $\sim 3600\text{--}10300\ \text{\AA}$, with a $400\ \text{\AA}$ overlap in the dichroic region (see Table 3 for details). The typical spectral resolution ranges from 1560 to 2650, and is a function of the wavelength, telescope focus, and the location of an individual fiber on each detector (see, e.g., Figure 37 of Smee et al. 2013); we discuss this further in Sections 4.2.5 and 10.2.

While each of the IFUs is assigned a specific plugging location on a given plate, the sky fibers are plugged non-deterministically (although all are kept within $14\ \text{arcmin}$ of the galaxy that they are associated with). Each cartridge is mapped after plugging by scanning a laser along the pseudo-slitheads and recording the corresponding illumination pattern on the plate. In addition to providing a complete mapping of fiber number to on-sky location, this also serves to identify any broken or misplugged fibers. This information is recorded in a central svn-based metadata repository called MANGACORE (see Section 3.3).

2.2. Operations

Each time a plate is observed, the cartridge on which it is installed is wheeled from a storage bay to the telescope and mounted at the Cassegrain focus. Observers acquire a given field using a set of 16 coherent imaging fibers that feed a guide

camera; these provide the necessary information to adjust focus, tracking, plate scale, and field rotation using bright guide stars throughout a given set of observations. In addition to simple tracking, constant corrections are required to compensate for variations in temperature and altitude-dependent atmospheric refraction.

At the start of each set of observations, the spectrographs are first focused using a pair of hartmann exposures; the best focus is chosen to optimize the line spread function (LSF) across the entire detector region (see Sections 4.2.2 and 4.2.5). Twenty-five-second quartz calibration lamp flat-fields and four-second Neon–Mercury–Cadmium arc-lamp exposures are then obtained by closing the eight flat-field petals covering the end of the telescope. These provide information on the fiber-to-fiber relative throughput and wavelength calibration, respectively; since both are mildly flexure dependent they are repeated every hour of observing at the relevant hour angle and declination.

After the calibration exposures are complete, science exposures are obtained in sets of three 15 minute dithered exposures. As detailed by Law et al. (2015), this integration time is a compromise between the minimum time necessary to reach background limited performance in the blue while simultaneously minimizing astrometric drift due to DAR between the individual exposures. Since MaNGA is an imaging spectroscopic survey, image quality is important and the 56% fill factor of circular fiber apertures within the hexagonal MaNGA IFU footprint (Law et al. 2015) naturally suffers from substantial gaps in coverage. To that end, we obtain data in “sets” of three exposures dithered to the vertices of an equilateral triangle with $1.44\ \text{arcsec}$ to a side. As detailed by Law et al. (2015), this provides optimal coverage of the target field and permits complete reconstruction of the focal plane image. Since atmospheric refraction (which is wavelength dependent, time-dependent through the varying altitude and parallactic angle, and field dependent through uncorrected quadrupole scale changes over our 3° field) degrades the uniformity of the effective dither pattern, each set of three exposures is obtained in a contiguous hour of observing.²⁵ These sets of three exposures are repeated until each plate reaches a summed signal-to-noise ratio (S/N) squared of $20\ \text{pixel}^{-1}\ \text{fiber}^{-1}$ in g -band at $g = 22\ \text{AB}$ and $36\ \text{pixel}^{-1}\ \text{fiber}^{-1}$ in i -band at $i = 21\ \text{AB}$ (typically 2–3 hr of total integration; see R. Yan et al. 2016b).

All MaNGA galaxy survey observations are obtained in dark or gray-time for which the moon illumination is less than 35% or below the horizon (see R. Yan et al. 2016b for details). Since MaNGA shares cartridges with the infrared SDSS-IV/APOGEE spectrograph, however (Wilson et al. 2010), both instruments are able to collect data simultaneously. MaNGA and APOGEE therefore typically co-observe, meaning that data are also obtained with the MaNGA instrument during bright-time with up to 100% moon illumination. These bright-time data are not dithered, have substantially higher sky backgrounds, and are generally used for ancillary science observations of bright stars with the aim of amassing a library of stellar reference spectra over the lifetime of SDSS-IV. These bright-time data are processed with the same MaNGA software

²⁵ In practice, weather constraints sometimes make this impossible. MaNGA scheduling software therefore takes into account observing conditions so that uniform-coverage sets can be assembled from exposures taken at similar hour angles on different nights.

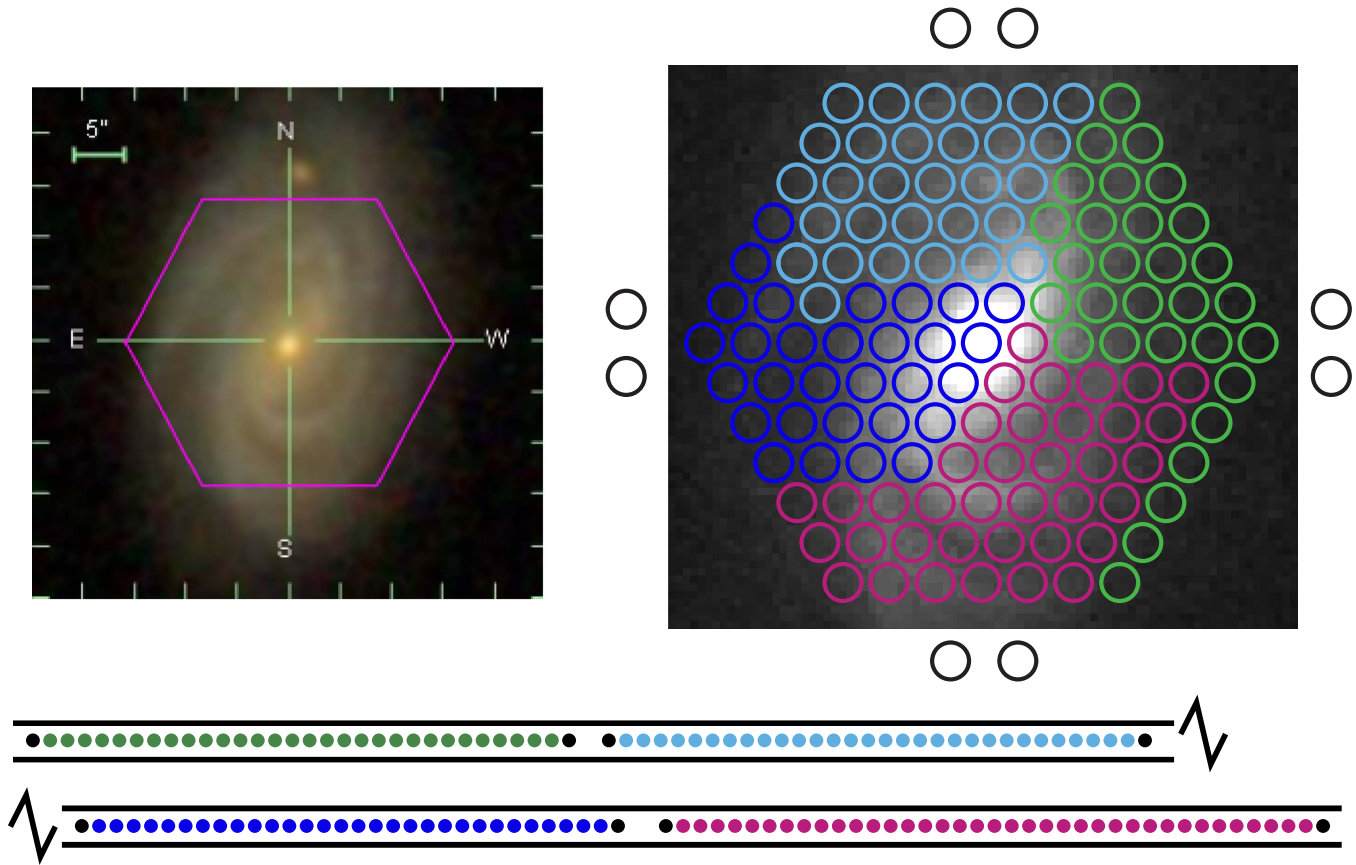


Figure 1. Schematic diagram of a 127 fiber IFU on MaNGA galaxy 7495–12704. The left-hand panel shows the SDSS three-color RGB image of the galaxy overlaid with a hexagonal bounding box showing the footprint of the MaNGA IFU. The right-hand panel shows a zoomed-in grayscale *g*-band image of the galaxy overlaid with circles indicating the locations of each of the 127 optical science fibers (colored circles) and schematic locations of the 8 sky fibers (black circles). These fibers are grouped into four physical blocks on the spectrograph entrance slit (schematic diagram at bottom), with the sky fibers located at the ends of each block. Note that the orientation of this figure is flipped in relation to Figure 9 of Drory et al. (2015) as the view presented here is on-sky (north up, east left).

Table 3
BOSS Spectrograph Detectors

	Blue Cameras	Red Cameras
Type	e2V	LBNL fully depleted
Grism (l/mm)	520	400
Wavel. Range (\AA) ^a	3600–6300	5900–10300
Resolution ^a	1560–2270	1850–2650
Detector Size	4352 × 4224	4352 × 4224
Active Pixels ^b	[128:4223, 56:4167]	[119:4232, 48:4175]
Pixel Size (μm)	15	15
Read noise (e-/pixel) ^a	~2.0	~2.5
Gain (e-/ADU) ^a	~1.0	~1.5–2.0

Notes.

^a Values are approximate; see Smee et al. (2013) for details.

^b Zero-indexed locations of active pixels between overscan regions.

pipeline as the dark-time galaxy data, albeit with some modifications and unique challenges that we will address in a future contribution.

3. OVERVIEW: MANGA DRP

In this section we give a broad overview of the MaNGA DRP and related systems in order to provide a framework for the detailed discussion of individual elements presented in Sections 4–9.

3.1. Data Reduction Pipeline

The MaNGA DRP is tasked with producing fully flux-calibrated data for each galaxy that has been spatially rectified and combined across all individual dithered exposures in a multi-extension FITS format that may be used for scientific analysis. This MANGADRP software is written primarily in IDL, with some C bindings for speed optimization and a variety of python-based automation scripts. Dependencies include the SDSS IDLUTILS and NASA Goddard IDL astronomy users libraries; namespace collisions with these and other common libraries have been minimized by ensuring that non-legacy DRP routines are prefixed by either “ml_” or “mdrp_.” The DRP runs automatically on all data using the collaboration supercluster at the University of Utah,²⁶ is publicly accessible in a subversion SVN repository at https://svn.sdss.org/public/repo/manga/mangadrp/tags/v1_5_4 with a BSD three-clause license, and has been designed to run on individual users’ home systems with relatively little overhead.²⁷ Version control of the MANGADRP code and dependencies is done via SVN repositories and traditional trunk/branch/tag methods; the version of MANGADRP described in the present contribution corresponds to tag v1_5_4 for public release DR13. We note that v1_5_4 is nearly identical to v1_5_1 (which has been used for SDSS-IV internal release MPL-4) save for minor

²⁶ Presently 27 nodes with 16 CPUs per node.

²⁷ Installation instructions are available at https://svn.sdss.org/public/repo/manga/mangadrp/tags/v1_5_4/pdf/userguide.pdf.

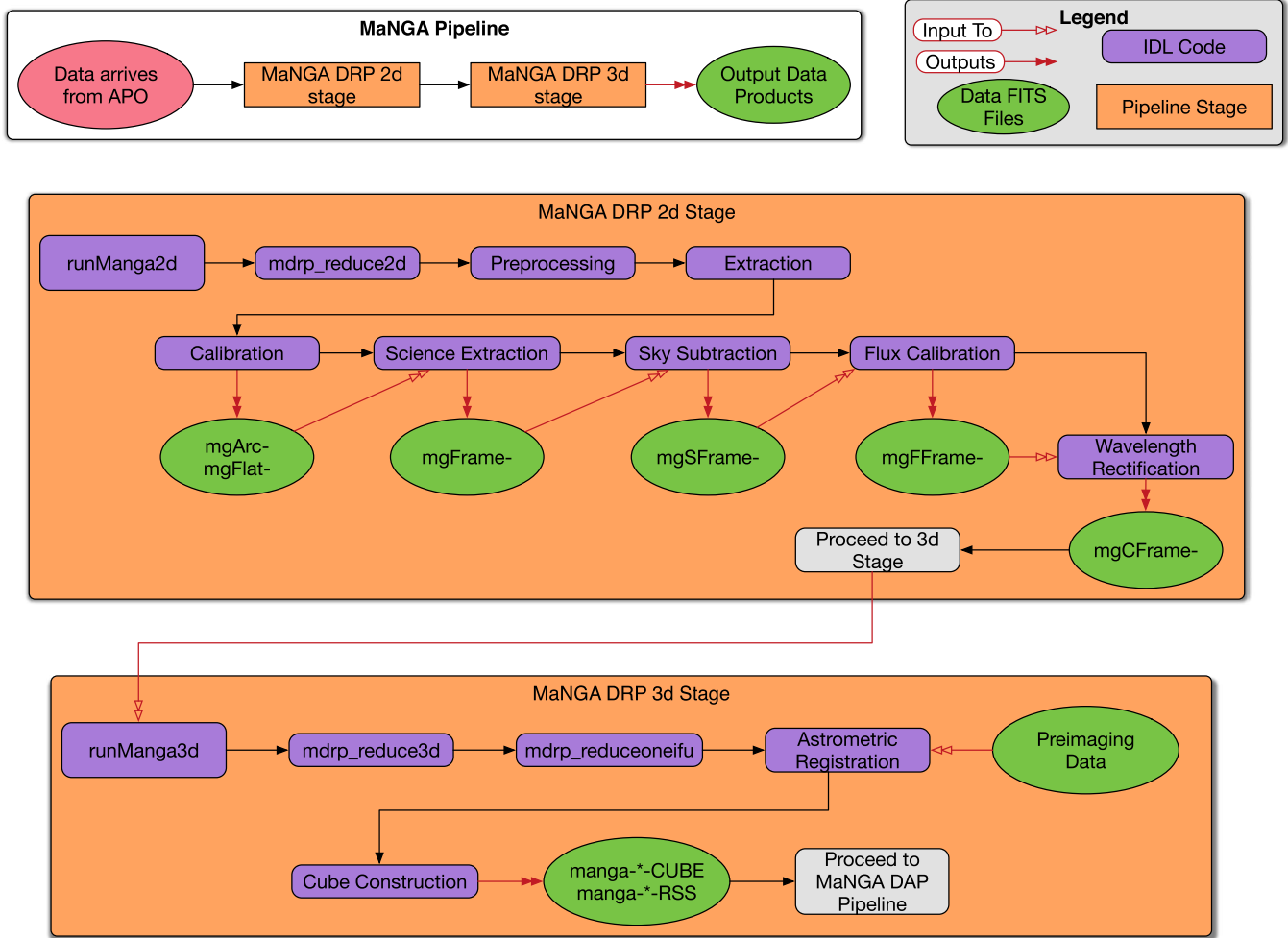


Figure 2. Schematic overview of the MaNGA data reduction pipeline. The DRP is broken into two stages: `mdrp_reduce2d` and `mdrp_reduce3d`. The 2D pipeline data products are flux-calibrated individual exposures corresponding to an entire plate; the 3D pipeline products are summary data cubes and row-stacked spectra for a given galaxy combining information from many exposures.

improvements in cosmic-ray rejection routines and data-quality-assessment statistics.

The DRP consists of two primary parts: the 2D stage that produces flux-calibrated fiber spectra from individual exposures, and the 3D stage that combines individual exposures with astrometric information to produce stacked data cubes. The overall organization of the DRP is illustrated in Figure 2. Each day when new data are automatically transferred from APO to the SDSS-IV central computing facility at the University of Utah a cronjob triggers automated scripts that run the 2D DRP on all new exposures from the previous modified Julian date (MJD). These are processed on a per-plate basis, and consist of a mix of science and calibration exposures (flat-fields and arcs).

The 2D stage of the MaNGA DRP is largely derived from the BOSS IDLSPEC2D pipeline (see, e.g., Dawson et al. 2013, Schlegel et al., in preparation)²⁸ that has been modified to address the different hardware design and science requirements of the MaNGA survey (we summarize the numerous differences in Appendix A). Each frame undergoes basic pre-processing to remove overscan regions and variable-quadrant bias before the one-dimensional

(1D) fiber spectra are extracted from the CCD detector image. The DRP first processes all of the calibration exposures to determine the spatial trace of the fiber spectra on the detector and extract fiber flat-field and wavelength calibration vectors, and applies these to the corresponding science frames. The science exposures are in turn extracted, flatfielded, and wavelength calibrated using the corresponding calibration files. Using the sky fibers present in each exposure we create a super-sampled model of the background sky spectrum, and subtract this off from the spectra of the individual science fibers. Finally, the 12 mini-bundles targeting standard stars in each exposure are used to determine the flux calibration vector for the exposure compared to stellar templates. The final product of the 2D stage is a single FITS file per exposure (`mgCFrame`) containing row-stacked spectra (RSS; i.e., a 2D array in which each row corresponds to an individual 1D spectrum) of each of the 1423 fibers interpolated to a common wavelength grid and combined across the four individual detectors.

Once a sufficient number of exposures has been obtained on a given plate, it is marked as complete at APO and a second automated script triggers the 3D stage DRP to combine each of the `mgCFrame` files resulting from the 2D DRP. For each IFU (including calibration mini-bundles) on the plate, the 3D pipeline identifies the relevant spectra in the `mgCFrame` files and assembles them into a master row-stacked format consisting of

²⁸ The IDLSPEC2D software has also been used for the DEEP2 survey; see Newman et al. (2013).

all spectra for that target. The astrometric solution as a function of wavelength for each of these spectra is computed on a per-exposure basis using the known fiber bundle metrology and dither offset for each exposure, along with a variety of other factors including field and chromatic differential refraction (see Law et al. 2015). This astrometric solution is further refined using SDSS broadband imaging of each galaxy to adjust the position and rotation of the IFU fiber coordinates. Using this astrometric information the DRP combines the fiber spectra from individual exposures into a rectified data cube and associated inverse variance and mask cubes. In post-processing, the DRP additionally computes mock broadband *griz* images derived from the IFU data, estimates of the reconstructed point-spread function (PSF) at *griz*, and a variety of quality-control metrics and reference information.

The final DRP data products in turn feed into the MaNGA Data Analysis Pipeline (DAP), which performs spectral modeling, kinematic fitting, and other analyses to produce science data products such as H α velocity maps, kinematics, spectral emission line ratio maps, etc., from the data cubes. DAP data products will be made public in a future release and described in a forthcoming contribution by K. Westfall et al. (in preparation).

3.2. Quick-reduction Pipeline (DOS)

Rather than running the full DRP in real-time at the observatory, we instead use a pared-down version of the code that has been optimized for speed that we refer to as DOS.²⁹ The DOS pipeline shares much of its code with the DRP, performing reduction of the calibration and science exposures up through sky subtraction. The primary difference is in the spectral extraction; while the DRP performs an optimized profile fitting technique to extract the spectra of each fiber (see Section 4.2.2), DOS instead uses a simple boxcar extraction that sacrifices some accuracy and robustness for substantial gains in speed.

The primary purpose of DOS is to provide real-time feedback to APO observers on the quality and depth of each exposure. Each exposure is characterized by an effective depth given by the mean S/N squared at a fixed fiber2mag³⁰ of 22 (*g*-band) and 21 (*i*-band). The S/N of each fiber is calculated empirically by DOS from the sky-subtracted continuum fluxes and inverse variances, while nominal fiber2mags for each fiber in a galaxy IFU are calculated by applying aperture photometry to SDSS broadband imaging data at the known locations of each of the IFU fibers (see Section 8.1) and correcting for Galactic foreground extinction following Schlegel et al. (1998). As illustrated in Figure 3, the S/N as a function of fiber2mag for all fibers in a given exposure forms a logarithmic relation that can be fitted and extrapolated to the effective achieved S/N at fixed nominal magnitudes $g = 22$ and $i = 21$. This calculation is done independently for all four cameras using a *g*-band effective wavelength range $\lambda\lambda 4000\text{--}5000\text{ \AA}$ and an *i*-band effective wavelength range $\lambda\lambda 6910\text{--}8500\text{ \AA}$. As described above in Section 2.2, we integrate on each plate until the cumulative S/N² in all complete sets of exposures

²⁹ Daughter-of-Spectro. This pipeline is a sibling to the Son-of-Spectro quick-reduction pipeline used by the BOSS and eBOSS surveys, both of which are descended from the original SDSS-I Spectro pipeline.

³⁰ Fiber2mag is a magnitude measuring the flux contained within a 2 arcsec diameter aperture; see http://www.sdss.org/dr13/algorithms/magnitudes/#mag_fiber.

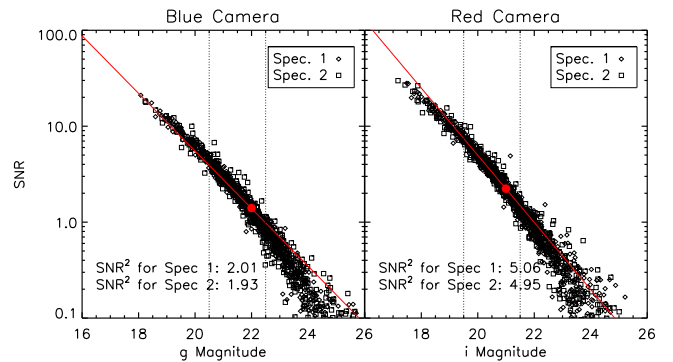


Figure 3. S/N as a function of extinction-corrected fiber magnitude for blue (left panel) and red cameras (right panel), for spectrographs 1 and 2 (diamond vs. square symbols, respectively). The red line indicates the logarithmic relation derived from fitting points in the magnitude range indicated by the vertical dotted lines. The filled red circle indicates the derived fit at the nominal magnitudes $g = 22$ and $i = 21$, with the S/N² values given for each spectrograph. This example corresponds to MaNGA plate 7443, MJD 56741, exposure 177378.

reaches $20\text{ pixel}^{-1}\text{ fiber}^{-1}$ in *g*-band and $36\text{ pixel}^{-1}\text{ fiber}^{-1}$ in *i*-band at the nominal magnitudes defined above.

3.3. Metadata

MaNGA is a complex survey that requires tracking of multiple levels of metadata (e.g., fiber bundle metrology, cartridge layout, fiber plugging locations, etc.), any of which may change on the timescale of a few days (in the case of fiber plugging locations) to a few years (if cartridges and/or fiber bundles are rebuilt). At any point, it must be possible to rerun any given version of the pipeline with the corresponding metadata appropriate for the date of observations. This metadata must also be used throughout the different phases of the survey from planning and target selection, to plate drilling, to APO operations, to eventual reduction and post-processing.

To this end, MaNGA maintains a central metadata repository MANGACORE, which is automatically synchronized between APO and the Utah data reduction hub using daily crontabs. Version control of files within MANGACORE is maintained by a combination of MJD timestamps and periodic SVN tags corresponding to major data releases (v1_2_3 for DR13).

3.4. Quality Control

Given the volume of data that must be processed by the MaNGA pipeline (~ 10 million reduced galaxy spectra and ~ 100 million raw-frame spectra over the six-year lifetime of SDSS-IV³¹), automated quality control is essential. To that end, multiple monitoring routines are in place. The 2D and 3D stage DRP has bitmasks (MANGA_DRP2PIXMASK and MANGA_DRP3PIXMASK, respectively) associated with the primary flux extensions that can be used to indicate individual pixels (or spaxels³² in the case of the 3D data cubes) that are identified as problematic. In the 2D case (spectra of all 1423 individual fibers within a single exposure), this pixel mask indicates such things as cosmic-ray events, bad flat-fields, missing fibers, extraction problems, etc. In the 3D stage (a

³¹ Assuming an average of three clear hours per night between the bright and dark-time programs, five exposures per hour (including calibrations), and ~ 3000 spectra per exposure among four individual CCDs.

³² Spatial picture element.

composite cube for a single galaxy that combines many individual exposures into a regularized grid), this pixel mask indicates things like low/no fiber coverage, foreground star contamination, and other issues that mean a given spaxel should not be used for science.

Additionally, there are overall quality bits MANGA_DRP2QUAL and MANGA_DRP3QUAL that pertain to an entire exposure or data cube, respectively, and indicate potential issues during processing. In the 2D case, this can include effects like heavy cloud cover, missing IFUs, or abnormally high scattered light. In the 3D case, this can include warnings for bad astrometry, bad flux calibration, or (rarely) a critical problem suggesting that a galaxy should not be used for science. As of DR13, 22 of the 1390 galaxy data cubes are flagged as critically problematic for a variety of reasons ranging from the severe and unrecoverable (e.g., poor focus due to hardware failure, ~ 5 objects) to the potentially recoverable in a future data release (e.g., failed astrometric registration due to a bright star at the edge of the IFU bundle) to the mundane (errant unflagged cosmic-ray confusing the flux calibration QA routine).

All of these pixel-level and exposure-level data quality flags are used by the pipeline in deciding how and whether to continue to process data (e.g., flux calibration will not be attempted on an exposure flagged as completely cloudy). We provide a reference table of the key MaNGA quality-control bitmasks in Appendix B.4.

4. SPECTRAL EXTRACTION

MaNGA exposures are differentiated from BOSS/eBOSS exposures taken with the same spectrographs using FITS header keywords, and a planfile³³ is created for each plate on a given MJD detailing each of the exposures obtained for which the quality was deemed by DOS at APO to be excellent. The MaNGA DRP parses this planfile and performs pre-processing, spectral extraction, flatfielding, wavelength calibration, sky subtraction, and flux calibration on a per-exposure basis.

4.1. Pre-processing

Raw data from each of the four CCDs (b1, r1, b2, r2) are in the format of 16 bit images with 4352 columns and 4224 rows (Table 3), with a 4096×4112 pixel active area (for the blue CCDs; 4114×4128 pixel active area for the red CCDs) and overscan regions along each edge of the detector. As described by Dawson et al. (2013), the CCDs are read out with four amplifiers, one for each quadrant, resulting in variable bias levels. Each exposure is preprocessed to remove the overscan regions of the detector, subtract off quadrant-dependent biases, convert from bias corrected ADUs to electrons using quadrant-dependent gain factors derived from the overscan regions,³⁴ and divide by a flat-field containing the relative pixel-to-pixel response measured from a uniformly illuminated calibration image (see Figure 4).

A corresponding inverse variance image is created using the measured read noise and photon counts in each pixel; this inverse variance array is capped so that no pixel has a reported

S/N greater than 100.³⁵ Finally, potential cosmic rays (which affect ~ 10 times as many pixels in the red cameras as in the blue) are identified and flagged using the same algorithm adopted previously by the SDSS imaging and spectroscopic surveys. As discussed by R. H. Lupton (see <http://www.astro.princeton.edu/~rhl/photo-lite.pdf>), this algorithm is a first-pass approach that successfully detects *most* cosmic rays by looking for features sharper than the known detector PSF, but sometimes incompletely flags pixels around the edge of cosmic-ray tracks. A second-pass approach that addresses these residual features is applied later in the pipeline, as described in Section 7. The inverse variance image is combined with this cosmic-ray mask and a reference bad pixel mask so that affected pixels are assigned an inverse variance of zero (and hence have zero weight in the reductions).

4.2. Calibration Frames

All flat-field and arc calibration frames from a planfile are reduced prior to processing any science frames. These provide estimates of the fiber-to-fiber flat-field and the wavelength solution, and are also critical for determining the locations of individual fiber spectra on the detectors. Since there are four cameras, each reduced flat-field (arc) exposure corresponds to four mgFlat (mgArc) multi-extension FITS files as described in the data model in Appendix B.

4.2.1. Spatial Fiber Tracing

As illustrated in Figure 4, MaNGA fibers are arranged into blocks of 21–39 fibers with 22 blocks on each spectrograph, with individual spectra running vertically along each CCD. The fiber spacing within blocks is $177 \mu\text{m}$ for science IFUs (~ 4 pixels), and $204 \mu\text{m}$ for spectrophotometric calibration IFUs, with $\sim 624 \mu\text{m}$ between each block. Fibers are initially identified in a uniformly illuminated flat-field image using a cross-correlation technique to match the 1D profile along the middle row of the detector against a reference file describing the nominal location of each fiber in relative pixel units. The cross-correlation technique matching against all fibers on a given slit allows for shifts due to flexure-based optical distortions while ensuring robustness against missing or broken individual fibers and/or entire IFUs. Fibers that are missing within the central row are flagged as dead in MANGACORE.

With the initial x -positions of each fiber in the central row thus determined, the centroids of each fiber in the other rows are then determined using a flux-weighted mean with a radius of 2 pixels. This algorithm sequentially steps up and down the detector from the central row, using the previous row's position as the initial input to the flux-weighted mean. Fibers with problematic centroids (e.g., due to cosmic rays) are masked out, and replaced with estimates based on neighboring traces. These flux-weighted centroids are further refined using a per-fiber cross-correlation technique matching a Gaussian model fiber profile (see Section 4.2.2) against the measured profile in a given row. This fine adjustment is required in order to remove sinusoidal variations in the flux-weighted centroids at the ~ 0.1 pixel level caused by discrete jumps in the pixels included in the previous flux-weighted centroiding.

Once the positions of all fibers across all rows of the detector have been computed, the discrete pixel locations are

³³ A planfile is a plaintext ascii file that is both machine and human readable (see <http://www.sdss.org/dr13/software/par/>) and contains a list of the science and calibration exposures to be processed through a given stage of the pipeline.

³⁴ Typical read noise and detector gains are given in Table 3; these are slightly different for each quadrant of each detector, and can evolve over the lifetime of the survey. See Smee et al. (2013) for details.

³⁵ This helps resolve problems arising when extracting extremely bright spectral emission lines.

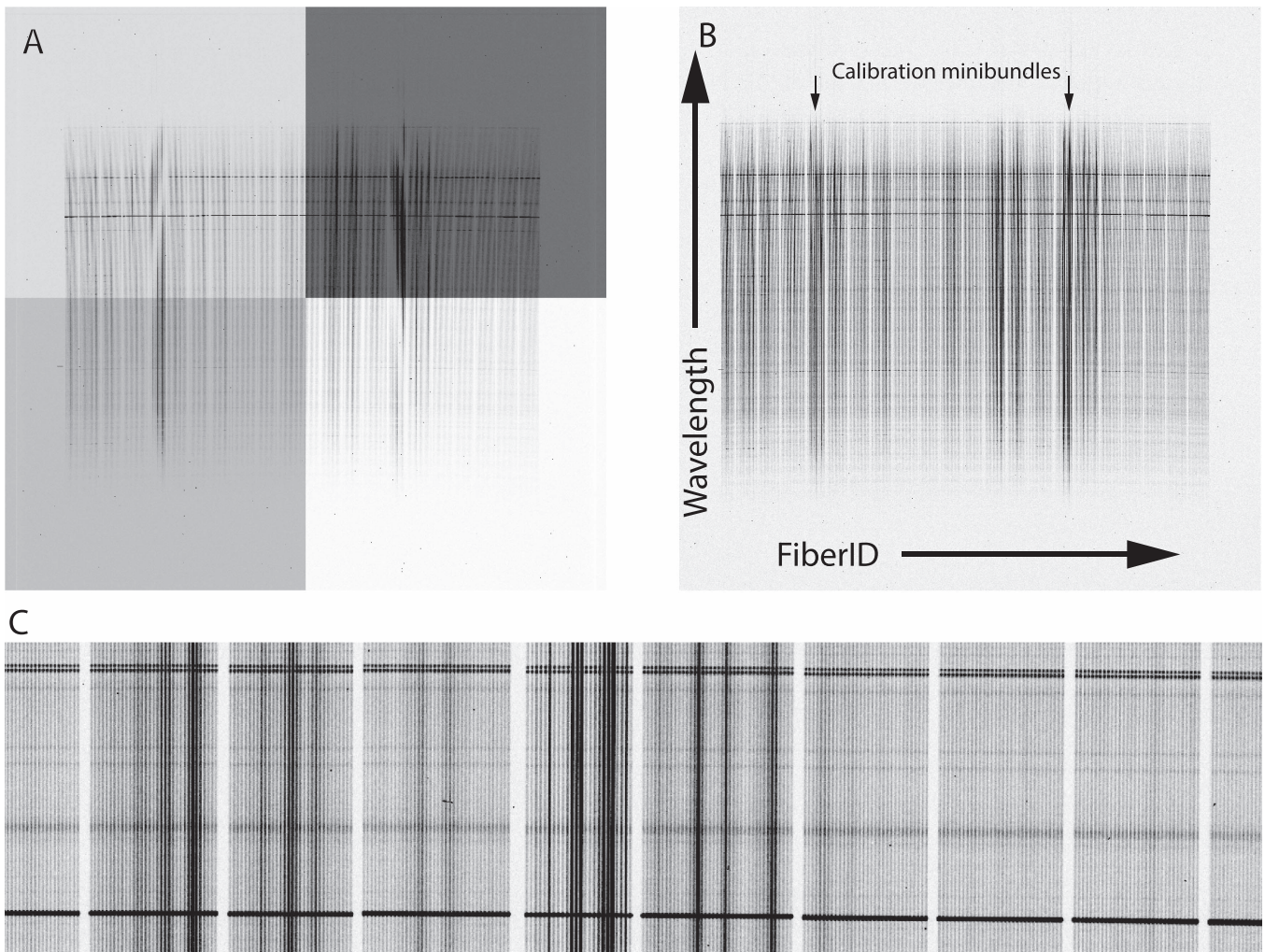


Figure 4. Illustration of the MaNGA raw data format before (A) and after (B) pre-processing to remove the overscan and quadrant-dependent bias. This image shows a color-inverted typical 15 minute science exposure for the b1 camera (exposure 177378 for plate 7443 on MJD 56741). There are 709 individual fiber spectra on this detector, grouped into 22 blocks. Bright spectra represent central regions of the target galaxies and/or spectrophotometric calibration stars; bright horizontal features are night-sky emission lines. Panel C zooms in on 10 blocks in the wavelength regime of the bright [O I 5577] skyline.

stored as a traceset³⁶ of seventh-order Legendre polynomial coefficients. An iterative rejection method accounts for scatter and uncertainty in the centroid measurement of individual rows and ensures realistically smooth variation of a given fiber trace as a function of wavelength along the detector. The best-fit traceset coefficients are stored as an extension in the per-camera mgFlat files (Table 5).

4.2.2. Spectral Extraction

Similarly to the BOSS survey (Dawson et al. 2013), we extract individual fiber spectra from the 2D detector images using a row-by-row optimal extraction algorithm that uses a least-squares profile fit to obtain an unbiased estimate of the total counts (Horne 1986). The counts in each row are modeled

by a linear combination of N_{fiber} Gaussian³⁷ profiles plus a low-order polynomial (or cubic basis-spline; see Section 4.2.3) background term. As we illustrate in Figure 5 (right panel), the resulting model is an extremely good fit to the observed profile. MaNGA uses the `extract_row.c` code (dating back to the original SDSS spectroscopic survey), which creates a pixelwise model of the Gaussian profile integrated over fractional pixel positions (i.e., the profile is assumed to be Gaussian prior to pixel convolution), describes deviations to the line centers and widths as linear basis modes (representing the first and second spatial derivatives, respectively), and solves for the banded matrix inversion by Cholesky decomposition. An initial fit to the flat-field calibration images allows both the amplitude and the width of the Gaussian profiles in each row to vary freely, with the centroid set to the positions determined via fiber tracing in Section 4.2.1. These individual width measurements are noisy, however, and for each block of fibers we therefore fit the derived widths with a linear relation as a function of fiberid along the slit in order to reject errant values and determine a fixed set of fiber widths that vary smoothly (within a given

³⁶ A traceset is a set of coefficient vectors defining functions over a common independent-variable domain specified by “xmin” and “xmax” values. The functions in the set are defined in terms of a linear combination of basis functions (such as Legendre or Chebyshev polynomials) up to a specified maximum order, weighted by the values in the coefficient vectors, and evaluated using a suitable affine rescaling of the dependent-variable domain (such as [xmin, xmax] \rightarrow [-1, 1] for Legendre polynomials). For evaluation purposes, the domain is assumed by default to be a zero-based integer baseline from xmin to xmax such as would correspond to a digital detector pixel grid.

³⁷ N_{fiber} is the number of fibers on a given detector ($N_{\text{fiber}} = 709$ for spectrograph 1, $N_{\text{fiber}} = 714$ for spectrograph 2).

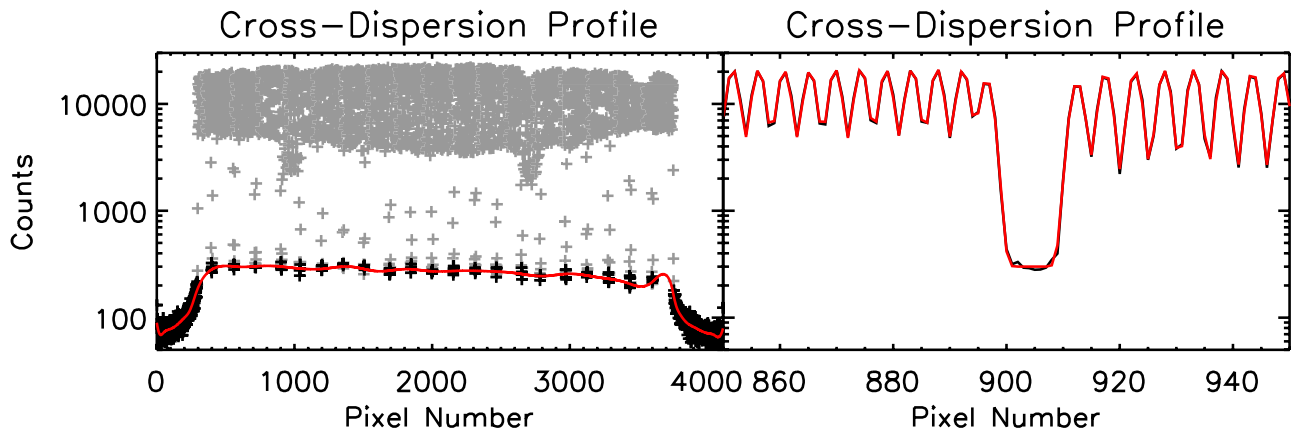


Figure 5. Left panel: cross-dispersion flat-field profile cut for the R1 camera. Gray points lie within five pixels of the measured fiber traces, black points are more than five pixels from the nearest fiber trace. The solid red line indicates the bspline fit to the inter-block values. Right panel: Cross-dispersion profile zoomed in around CCD column 900. The solid black line shows the individual pixel values, the solid red line overplots the Gaussian profile fiber fit plus the bspline background term convolved with the pixel boundaries. The trough around pixel 900–910 represents a gap between V-groove blocks. Both panels show row 2000 from plate 8069 observed on MJD 57278.

block) with both fiberid and wavelength. As illustrated in Figure 6, low-frequency variation of the widths with fiberid reflects the telescope focus (which we choose to ensure that the widths are as constant as possible across the entire slit), while discontinuities at the block boundaries are due to slight differences in the slithead mounting. These fixed widths are then used in a second fit to the detector images in which only the polynomial background and the amplitude of the Gaussian terms are allowed to vary.

The final value adopted for the total flux in each row is the integral of the theoretical Gaussian profile fits to the observed pixel values, while the inverse variance is taken to be the diagonal of the covariance matrix from the Cholesky decomposition. This approach allows us to be robust against cosmic rays or other detector artifacts that cover some fraction of the spectrum, since unmasked pixels in the cross-dispersion profile can still be used to model the Gaussian profile (Figure 5). Additionally, this technique naturally allows us to model and subtract crosstalk arising from the wings of a given profile overlapping any adjacent fibers, and to estimate the variance on the extracted spectra at each wavelength. This step transforms our 4096×4112 CCD images (4114×4128 for the red cameras) to RSS with dimensionality $4112 \times N_{\text{fiber}}$ ($4128 \times N_{\text{fiber}}$ for the red cameras).

4.2.3. Scattered Light

The DRP automatically assesses the level of scattered light in the MaNGA data by taking advantage of the hardware design in which gaps of ~ 16 pixels were left between each v-groove block (compared to ~ 4 pixels peak-to-peak between each fiber trace within a block) so that the interstitial regions contain negligible light from the Gaussian fiber profile cores (Drory et al. 2015). By masking out everything within five pixels of the fiber traces we can identify those pixels on the edge of the detector and in empty regions between individual blocks whose counts are dominated by diffuse light on the detector. This light is a combination of (1) genuine scattered light that enters the detector via multiple reflections from un baffled surfaces and (2) highly extended non-Gaussian wings to the individual fiber profiles that can extend to hundreds of pixels and contain $\sim 1\%$ – 2% of the total light of a given fiber.

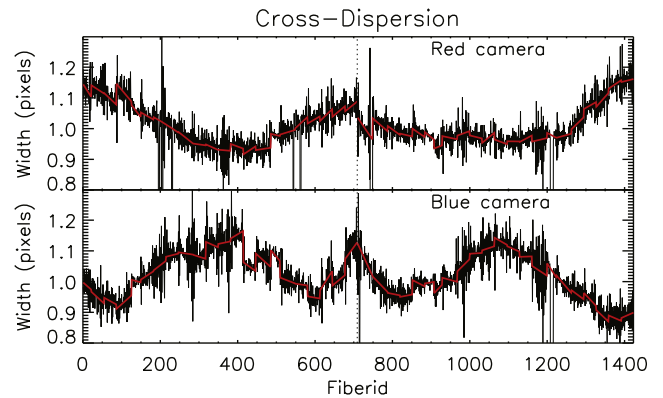


Figure 6. Example spatial width (1σ) for the cross-dispersion Gaussian fiber profile as a function of fiberid for the middle row of all four cameras. This example is for plate 8618, observed on MJD 57199. The solid black line represents individual measurements for each fiber in this row; the solid red line represents the adopted fit that assumes smooth variation of the widths with wavelength and as a function of fiberid within each block. The vertical dotted line represents the transition between the first and second spectrographs (fiberid 1–709 and 710–1423). Similar plots are produced automatically by the DRP for each flat-field processed, and are used for quality control.

For MaNGA dark-time science exposures (which typically peak at about $30 \text{ counts pixel}^{-1} \text{ fiber}^{-1}$ for the sky continuum) both components are small and can be satisfactorily modeled by a low-order polynomial term in each extracted row. For some bright-time exposures used in the stellar library program, however, the moon illumination can approach 100% and produce larger scattered light counts \sim a quarter of the sky background seen by individual fibers. Additionally, for our flat-field calibration exposures the summed contribution of the non-Gaussian wings to the fiber profiles can reach $\sim 300 \text{ counts pixel}^{-1}$ in the interstitial regions between blocks (compared to $\sim 20,000 \text{ counts pixel}^{-1}$ in the fiber profile cores). In both cases the simple polynomial background term can prove unsatisfactory, and we instead fit the counts in the interstitial regions row-by-row with a fourth-order basis-spline model that allows for a greater degree of spatial variability in the background than is warranted for the dark-time science exposures. This bspline model is evaluated at the locations of each intermediate pixel and smoothed along the detector columns by use of a 10 pixel

moving boxcar to mitigate the impact of individual bad pixels. The resulting bspline scattered light model is subtracted from the raw counts before performing spectral extraction.

4.2.4. Fiber Flat-field

Each flat-field calibration frame is extracted into individual fiber spectra using the above techniques and matched to the nearest (in time) arc-lamp calibration frame, which has been processed as described in Section 4.2.5. Using the wavelength solutions derived from the arc frames, we combine the individual flat-field spectra (first normalized to a median of unity) into a single composite spectrum with substantially greater spectral sampling than any individual fiber.³⁸ We fit this composite spectrum with a cubic basis-spline function to obtain the superflat vector describing the global flat-field response (i.e., the quartz lamp spectrum convolved with the detector response and system throughput). This global superflat is shown in Figure 7, and illustrates the falloff in system throughput toward the wavelength extremes of the detector (see also Figure 4 of Yan et al. 2016a).

We evaluate the superflat spline function on the native wavelength grid of each individual fiber and divide it out from the individual fiber spectra in order to obtain the relative fiber-to-fiber flat-field spectra. So normalized, these fiber-to-fiber flat-field spectra have values near unity, vary only slowly (if at all) with wavelength, and easily show any overall throughput differences between the individual fibers. Each such spectrum is in turn fitted with a bspline in order to minimize the contribution of photon noise to the resulting fiber flats and interpolate across bad pixels. In the end, we are left with two flat-fields to store in the mgFlat files (see Table 5); a single *superflat* spectrum describing the global average response as a function of wavelength, and a *fiberflat* of size $4112 \times N_{\text{fiber}}$ ($4128 \times N_{\text{fiber}}$ for the red cameras) describing the relative throughput of each individual fiber as a function of wavelength.

The individual MaNGA fibers typically have high throughput (see discussion by Drory et al. 2015) within 5%–10% of each other. The relative distribution of throughputs is monitored daily to trigger cleaning of the IFU surfaces when the DRP detects noticeable degradation in uniformity or overall throughput. Individual fibers with throughput less than 50% that of the best fiber on a slit are flagged by the pipeline and ignored in the data analysis. This may occur when a fiber and/or IFU falls out of the plate (a rare occurrence), or when a fiber breaks. Such breakages in the IFU bundles occur at the rate of about 1 fiber per month across the entire MaNGA complement of 8539 fibers.

4.2.5. Wavelength and Spectral Resolution Calibration

The Neon–Mercury–Cadmium arc-lamp spectra are extracted in the same manner as the flat-fields, except that they use the fiber traces determined from the corresponding flat-field (with allowance for a continuous 2D polynomial shift in the traces as a function of detector position to account for flexure differences) and allow only the Gaussian profile amplitudes to vary. These spectra are normalized by the fiber flat-field³⁹ and an initial wavelength solution is computed as follows.

³⁸ Since each fiber has a slightly different wavelength solution we effectively supersample the intrinsic input spectrum.

³⁹ In practice this is iterative; the flat-fields prior to separation of the superflat and fiberflat are used to normalize the arc-lamp spectra, the wavelength solution from which in turn allows construction of the superflat.

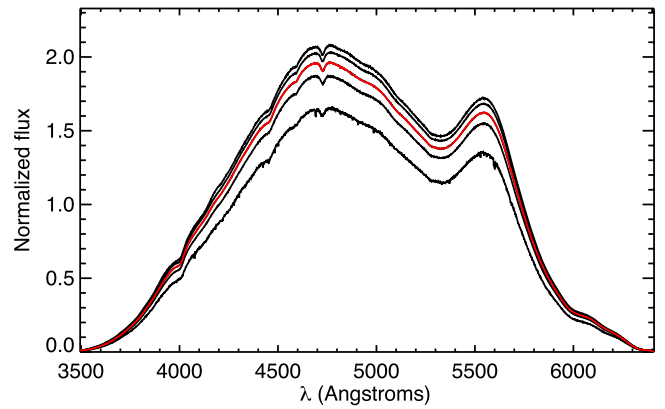


Figure 7. Example of a typical superflat spectrum for the b1 camera normalized to a median of unity. The solid red line shows the superflat fit to the median fiber, solid black lines indicate the 1σ and 2σ deviations about this median.

A representative spectrum is constructed from the median of the five closest spectra closest to the central fiber on the CCD. This spectrum is cross-correlated with a model spectrum generated using a reference table of known strong emission features in the Neon–Mercury–Cadmium arc lamps,⁴⁰ and iterated to determine the best-fit coefficients to map pixel locations to wavelengths. These best-fit coefficients are used to construct initial guesses for the wavelength solution of each fiber, which are then iterated on a fiber-to-fiber basis to obtain the final wavelength solutions. Several rejection algorithms are run to ensure reliable arc-line centroids across all fibers. A final sixth-order Legendre polynomial fit converts the wavelength solutions into a series of polynomial traceset coefficients. The higher order coefficients are forced to vary smoothly as a function of fiberid since they predominantly arise from optical distortions along the slit (whereas lower order terms represent differences arising from the fiber alignment). These coefficients are stored as an extension in the output mgArc file (see Table 4), and are used to reconstruct the wavelength solutions at all fibers and positions on the CCD.

The arc-lamp spectral resolution (hereafter the line spread function, or LSF) is computed by fitting the extracted spectra around the strong arc-lamp emission lines in each fiber with a Gaussian profile integrated over each pixel (note that we *integrate* the fitted profile shape across each pixel rather than simply *evaluating* the profile at the pixel midpoints; see the discussion in Section 10.2) and allowing both the width and amplitude of the profile to vary. As illustrated in Figure 8, these widths are intrinsically noisy and the DRP therefore fits them with a linear relation as a function of fiberid along the slit in order to reject errant values and determine a fixed set of line widths that vary smoothly (within a given block) with fiberid. These arc-line widths are then fit with a Legendre polynomial traceset that is stored in the mgArc files and evaluated at each pixel to compute the LSF at wavelengths between the bright arc lines.

Both wavelength and LSF solutions derived from the arc frames are later adjusted for each individual science frame to account for instrumental flexure during and between (see discussion in Section 4.3).

⁴⁰ There are ~ 50 such features with counts in the range 10^3 – 10^5 pixel $^{-1}$ in each of the blue and red cameras; see full list at https://svn.sdss.org/public/repo/manga/mangadrp/tags/v1_5_4/etc/lamphgcdne.dat.

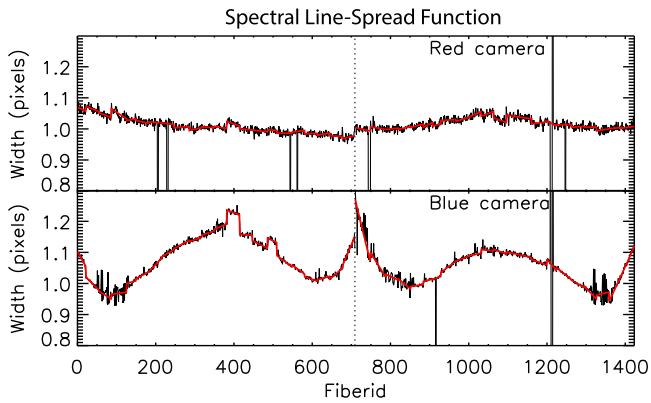


Figure 8. As Figure 6, but showing the spectral line spread function (1σ LSF) for the Gaussian arc-line profile as a function of fiberid for an emission line near the middle row of all four detectors (Cd I 5085.822 Å for the blue cameras, Ne I 8591.2583 Å for the red cameras).

All calibrations are additionally complicated in the red cameras since the middle row of pixels on these detectors is oversized by a factor of $1/3$, causing a discontinuity in both the wavelength solution and the LSF for each fiber as a function of pixel number. All of the algorithms described above therefore allow for such a discontinuity across the CCD quadrant boundary. The primary impact of this discontinuity on the final data products is to produce a spike of low spectral resolution around 8100 Å, the exact wavelength of which can vary from fiber to fiber based on the curvature of the wavelength solution along the detector.

4.3. Science Frames

Each science frame is associated with the arc and flat pair taken closest to it in time (generally within one hour since calibration frames are taken at the start of each plate and periodically thereafter), and extracted row-by-row following the method outlined in Section 4.2.2. During this extraction only the profile amplitudes and background polynomial term are allowed to vary freely; the trace centroids are tied to the flat-field traces with a global 2D polynomial shift to account for instrument flexure, and the cross-dispersion widths are fixed to the values derived from the flat-field. The extracted spectra are normalized by the superflat and fiberflat vectors derived from the flat-field.

The wavelength solutions derived from the arcs are adjusted for each science frame to match the known wavelengths of bright night-sky emission lines in the science spectra by fitting a low-order polynomial shift as a function of detector position to allow for instrumental flexure (these shifts are typically less than a quarter pixel). The final wavelength solution for each exposure is corrected to the vacuum heliocentric restframe using header keywords recording atmospheric conditions and the time and date of a given pointing. As we explore in Section 10.3, we achieve a $\sim 10 \text{ km s}^{-1}$ or better rms wavelength calibration accuracy with zero systematic offset to within 2 km s^{-1} .

Similarly, in order to account for flexure and varying spectrograph focus with time the spectral LSF measurements derived from the arc-lamp exposures are also adjusted for each science frame to match the LSF of bright skylines that are known to be unblended in high-resolution spectra (e.g., Osterbrock et al. 1996). Starting from the original arc-line

LSF model, we derive a quadrature correction term for the profile widths $Q^2 = \sigma_{\text{sky}}^2 - \sigma_{\text{arc}}^2$. Q is taken to be constant as a function of wavelength for each camera, and is based on the strong auroral O I 5577 line in the blue (since the Hg I lines are too weak and broadened to obtain a reliable fit) and an average of many isolated bright lines in the red.⁴¹ The measured quadrature correction term is fitted with a cubic basis-spline to ensure that the correction applied varies smoothly with fiberid. Across the ~ 1100 individual exposures in DR13 the average correction $Q^2 = 0.08 \pm 0.04 \text{ pixel}^2$ in the blue cameras and $Q^2 = 0.05 \pm 0.02 \text{ pixel}^2$ in the red cameras (likely due to the flatter and more stable focus in the red cameras).

The final RSS, inverse variances, pixel masks, wavelength solutions, and broadened LSF are all stored as extensions in the output mgFrame FITS file (Table 6).

5. SKY SUBTRACTION

Unlike previous SDSS spectroscopic surveys targeting bright central regions of galaxies, MaNGA will explore out to ≥ 2.5 effective radii (R_e) where galaxy flux is decreasing rapidly relative to the sky background. As illustrated in Figure 9, this night-sky background is especially bright at near-IR wavelengths longward of $\sim 8000 \text{ Å}$, where bright emission lines from OH radicals (e.g., Rousselot et al. 2000) dominate the background flux. These OH features vary in strength with both time and angular position depending on the coherence scale of the atmosphere, posing challenges for measuring faint stellar atmospheric features such as the Wing–Ford (Wing & Ford 1969) band of iron hydride absorption lines around 9900 Å. In many cases such faint features will be detectable only in stacked bins of spectra, driving the need to reach the Poisson-limited noise regime so that stacked spectra are not limited by systematic sky subtraction residuals.

We therefore design our approach to sky subtraction with the aim of reaching Poisson-limited performance at all wavelengths from $\lambda\lambda 4000\text{--}10000 \text{ Å}$ (beyond which the increasing read noise of the BOSS cameras prohibits such performance). Our sky subtraction algorithm is closely based on the routines developed for the BOSS survey, and relies on using the dedicated 92 sky fibers (46 per spectrograph) on each plate to construct a highly sampled model background sky that can be subtracted from each of the science fibers. These sky fibers are plugged into regions identified during the plate design process as blank sky “objects” within a 14 arcmin patrol radius of their associated IFU fiber bundle (see Figure 1).

5.1. Sky Subtraction Procedure

Sky subtraction is performed independently for each of the four cameras using the flat-fielded, wavelength-calibrated fiber spectra contained in the mgFrame files, and is a multi-step iterative process. Broadly speaking, we build a super-sampled sky model from all of the sky fibers, scale it to the sky background level of a given block, and evaluate it on the native solution of each fiber within that block. In detail:

1. The metadata associated with the exposure are used to identify the N_{sky} individual sky fibers in each frame based on their FIBERTYPE.

⁴¹ See https://svn.sdss.org/public/repo/manga/mangadrp/tags/v1_5_4/etc/skylines.dat for a complete list.

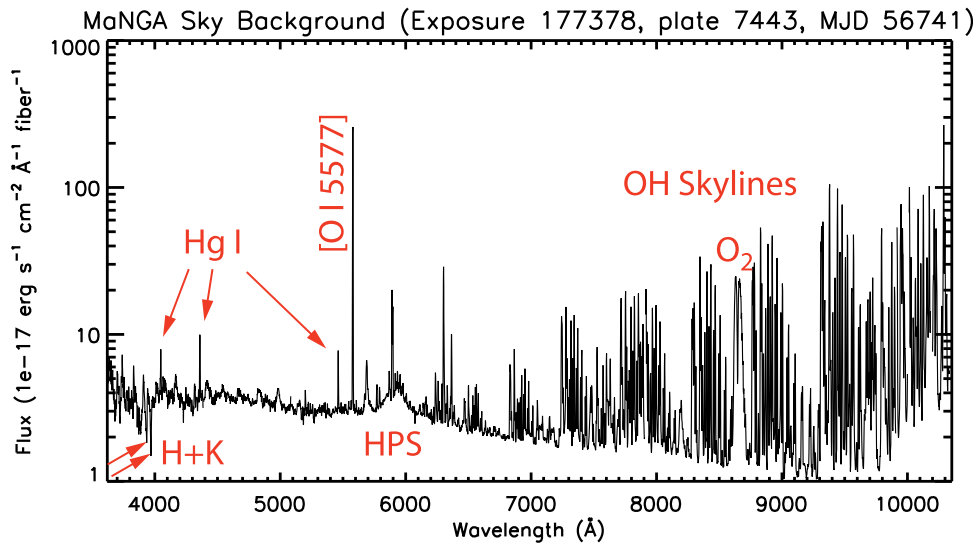


Figure 9. Typical flux-calibrated MaNGA night-sky background spectrum seen by a single optical fiber (2 arcsec core diameter). Bright features longward of 7000 Å represent blended OH and O₂ skyline emission (see, e.g., Osterbrock et al. 1996). The bright feature at 5577 Å is atmospheric [O I], the broad feature around 6000 Å is high-pressure sodium (HPS) from streetlamps; Hg I from Mercury vapor lamps contributes most of the discrete features at short wavelengths (see, e.g., Massey & Foltz 2000). Absorption features around 4000 Å are zodiacal Fraunhofer H and K lines.

2. Pixel values for these N_{sky} sky fibers are resorted as a function of wavelength into a single one-dimensional array of length $N_{\text{sky}} \times N_{\text{spec}}$ (where N_{spec} is the length of a single spectrum). Since each fiber has a unique wavelength solution, this super-sky vector has much higher effective sampling of the night-sky background spectrum than any individual fiber and provides an accurate LSF for OH airglow features. An example of this procedure is shown in Figure 10.
3. Similarly, we also construct a super-sampled weight vector by combining individual sky fiber *inverse variance spectra* that have first been smoothed by a boxcar of width 100 pixels ($\sim 100\text{--}200$ Å) in the continuum and 2 pixels ($\sim 2\text{--}3$ Å) within 3 Å of bright atmospheric emission features.
4. The super-sky spectrum is then weighted by the smoothed inverse variance spectrum (convolved with the bad-pixel mask) and fitted with a cubic basis-spline as a function of wavelength, with the number of breakpoints set to $\sim N_{\text{spec}}$ so that high-frequency variations (due, e.g., to shot noise or bad pixels) are not picked up by the resulting model (see, e.g., green line in Figure 10).⁴² The breakpoint spacing is set automatically to maintain approximately constant S/N between breakpoints. The B-spline fit itself is iterative, with upper and lower rejection thresholds set to mask bad or deviant pixels. We note that the smoothing of the inverse variance in determining the weight function is critical as otherwise the weights (which are themselves estimated from the data) would modulate with the Poisson scatter and bias the fit toward slightly lower values, resulting in systematic under-subtraction of the sky background, especially near the wavelength extrema where the overall system throughput is low.
5. This B-spline function is evaluated on the native wavelength solution of each of the sky fibers. Dividing the original sky fiber spectra by this functional model, and collapsing over wavelengths using a simple mean, we arrive at a series of scale factors describing the relative sky background seen by the fiber compared to all other fibers on the detector. For each harness (i.e., each IFU plus associated sky fibers) we compute the median of these scale factors to obtain a single averaged scale factor for each harness. These scale factors help account for nearly gray variations in the true sky continuum across our large field produced by a combination of intrinsic background variations and patchy cloud cover. The variability in sky background between harnesses is about 1.5% rms, with some larger deviations $>5\%$ observed during the bright-time stellar library program when pointing near a full moon can produce strong background gradients.
6. Repeat steps 2–4 after first scaling each individual sky fiber spectrum by the value appropriate for its harness in order to obtain a super-sky spectrum in which per-harness scaling effects have been removed.
7. Evaluate the new B-spline function on the native pixelized wavelength solution of each fiber (sky plus science), and multiply it by the scaling factor for the harness to obtain the first-pass model sky spectrum for each fiber. Subtract this from the spectra to obtain the first-pass sky-subtracted spectra.
8. Identify deviant sky fibers in which the median sky-subtracted residual $S/N^2 > 2$ (this is extremely rare, and generally corresponds to a case where a sky fiber location was chosen poorly, or a fiber was misplugged and not corrected before observing). Eliminate these sky fibers from consideration, and repeat steps 2–7 to obtain the second-pass model sky spectrum for each fiber. We refer to this as the 1D sky model.
9. Repeat steps 2–4, this time allowing the bspline fit to accommodate a smoothly varying third-order polynomial of values at each breakpoint as a function of fiberid (i.e., rather than requiring the model to be constant for all fibers, it is allowed to vary slowly as a function of slit position). This polynomial term is introduced in order to model

⁴² The number of breakpoints is reduced slightly in the blue cameras as there are few narrow spectral features that need to be fit.

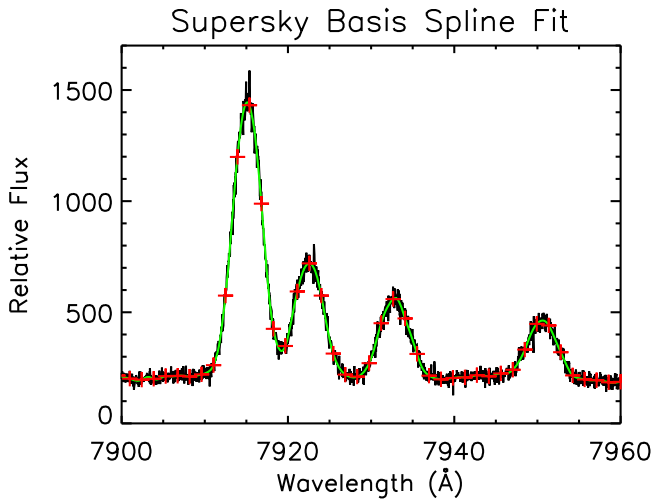


Figure 10. Example MaNGA super-sky spectrum created by the wavelength-sorted combination of all-sky fiber spectra (black line) in the OH-emission dominated wavelength region $\lambda\lambda 7900\text{--}7960$ Å. Overlaid in green is the b-spline model fit to the super-sky spectrum; red points represent the b-spline model after evaluation on the native pixelized wavelength solution of a single fiber.

variations in the LSF along each slit; empirically, increasing polynomial orders up to three results in an improvement of the skyline residuals, while no further gains are observed at greater than third order. Evaluate the new B-spline function on the native pixelized wavelength solution of each fiber (sky plus science) to obtain the 2D sky model. Notably, this 2D model does not use the explicit scaling used by the 1D model. This is partially because a similar degree of freedom is introduced by the 2D polynomial, and partially because OH features can vary in strength independently from the underlying continuum background (see, e.g., Davies 2007).

- The final sky model is a piecewise hybrid of the 1D and 2D models; in continuum regions it is taken to be the 1D model, and in the skyline regions (i.e., within 3 Å of any wavelength for which the sky background is $>5\sigma$ above a bspline fit to the interline continuum) it is taken to be the 2D model. We opt for this hybrid model as it optimizes our various performance metrics: In the continuum far from night-sky lines, our performance is limited by the poisson-based rms of the model sky spectrum subtracted from each science fiber. Therefore, we use the 1D model that is based on all 46 sky fibers on a given spectrograph. In contrast, for near bright skylines our performance is instead limited by our ability to accurately model the shape of the skyline wings, which can vary along the slit (see, e.g., Figure 8). Therefore, in skyline regions we use the 2D model, which improves the model LSF fidelity at the expense of some S/N. There is no measurable discontinuity between the sky-subtracted spectra at the piecewise 1D/2D model boundaries.

The final sky model is subtracted from the mgFrame spectra; these sky-subtracted spectra are stored in mgSFrame files (Table 7), which contain the spectra, inverse variances (with appropriate error propagation), pixel masks, applied sky models, etc. in a row-stacked format identical to the input mgFrame files.

5.2. Sky Subtraction Performance: All-sky Plates

We estimate the accuracy of our calibration and sky subtraction up to this point by using specially designed “all-sky” plates in which every science IFU is placed on a region of sky determined to be empty of visible sources according to the SDSS imaging data (calibration mini-bundles are still placed on standard stars so that these all-sky plates can be properly flux calibrated). The resulting sky-subtracted sky spectra can then be used to estimate the accuracy of our noise model, extraction algorithms, and sky-subtraction technique.

Working with the row-stacked mgSFrame spectra (i.e., prior to flux calibration and wavelength rectification) we construct “Poisson ratio” images for each camera by multiplying the sky-subtracted residual counts by the square root of the inverse variance (which accounts for both shot noise and detector read noise). If the sky subtraction is perfect, and the noise model properly estimated, these poisson ratio images should be devoid of structure with a Gaussian distribution of values with mean of 0 and $\sigma = 1.0$. In Figure 11 (right-hand panels) we show the actual distribution of values for the sky-subtracted science fibers for exposure 183643 (cart 4, plate 8069, MJD 56901) for each of the four cameras (solid black lines) compared to the ideal theoretical expectations (solid red line; note that this is *not* a fit to the data). We find that the overall distribution of values is broadly consistent with theoretical models in all four cameras (c.f. Figure 23 of Newman et al. 2013, which shows similar plots for the DEEP2 survey), albeit with some evidence for slight oversubtraction on average and a non-Gaussian wing in the blue cameras (pixels in this asymmetric wing do not correspond to particular wavelengths or fiberid).

We examine this behavior as a function of wavelength in Figure 11 (left-hand panel) by plotting the 1σ width of the Gaussian that best fits the distribution of unflagged pixel values at a given wavelength across all science fibers.⁴³ As before, perfectly noise-limited sky subtraction with a perfect noise model would correspond to a flat distribution of σ around 1.0 at all wavelengths; we note that the blue cameras and the continuum regions of the r2 camera are close to this level of performance with up to a 3% offset from nominal (suggesting that the read noise in some quadrants may be marginally underestimated). In the r1 camera the read noise may be overestimated by $\sim 10\%$ in some quadrants (as $\sigma < 1$ for r1 in the wavelength range $\lambda\lambda 5700\text{--}7600$ Å), but is otherwise well-behaved in the continuum region. In the skyline regions of the red cameras, performance is within 10% of Poisson expectations out to ~ 8500 Å. Longward of ~ 8500 Å (where skylines are brighter, and the spectra have greater curvature on the detectors) sky subtraction performance in skyline regions is $\sim 10\text{--}20\%$ above theoretical expectations. This is likely due to systematic residuals in the subtraction caused by block-to-block variations in the spectral LSF that are difficult to model completely. Indeed, such an analysis during commissioning revealed the OH skyline residuals were significantly worse in R1 than in the R2 camera. This led to the discovery of an optical coma in R1 that was fixed during Summer 2014 prior to the formal start of SDSS-IV, but which nonetheless affected the commissioning plates 7443 and 7495.

⁴³ Since each fiber has a different wavelength solution we cannot simply use all pixels in a given column, and therefore instead use the three pixels whose wavelengths are closest to a given wavelength in each fiber.

Overall, the results in Figure 11 indicate excellent performance from the MaNGA DR13 data pipeline sky subtraction, albeit with some room for further improvement in future data releases. Finally, we assess whether any systematics exist within the data that would prohibit stacking of multiple fiber spectra in order to reach faint surface brightness levels (e.g., in the outer regions of the target galaxies). Using the flux-calibrated, camera-combined mgCFrame data (again corresponding to exposure 183643 from MJD 56901) we compute the limiting 1σ surface brightness reached in the largely skyline-free wavelength range 4000–5500 Å as a function of the number of individual fiber spectra stacked. As shown in Figure 12, when N fibers are stacked randomly from across both spectrographs (solid black line) the limiting surface brightness decreases as $\sqrt{N^{-1} + 92^{-1}}$ (i.e., improving as \sqrt{N} for small N , and becoming limited by the statistics of the 92 fiber sky model as N becomes large). If fibers are stacked sequentially along the slit (dashed black line) the limiting surface brightness decreases as $\sqrt{N^{-1} + 46^{-1}}$ at first (since only the 46 sky fibers on a single slit are being used in the sky model) but approaches nominal performance again once fibers from both spectrographs are included in the stack ($N > 621$).

5.3. Sky Subtraction Performance: Skycorr

Another way to check the sky subtraction quality of the DRP is to compare its performance for a typical galaxy plate against the results obtained using the skycorr tool (Noll et al. 2014). Skycorr was designed as a data reduction tool to remove sky emission lines for astronomical spectra using physically motivated scaling relations, and has been found to consistently perform better than the popular algorithm of Davies (2007). As input, skycorr needs the science spectrum and a sky spectrum, preferably taken around the time as the science spectrum. After subtracting the continuum from both spectra, it then scales the sky emission lines from the sky spectrum to fit these lines in the science spectrum by comparing groups of sky lines that should vary in similar ways.

In Figure 13 we compare a typical sky-subtracted MaNGA science spectrum obtained using the DRP algorithms described in Section 5 with the spectrum obtained using skycorr instead. The two sky-subtracted spectra are nearly indistinguishable, indicating comparable performance between the two techniques.

6. FLUX CALIBRATION

Flux calibration for MaNGA (Yan et al. 2016a) has a different goal than in previous generations of SDSS spectroscopic fiber surveys. The goal for single-fiber flux calibration is often to retrieve the total flux of a point-like source, accounting for both flux lost due to atmospheric attenuation (or instrumental response) and the flux lost due to the fraction of the PSF that falls outside the fiber aperture. In contrast, IFU observations provide a *sampling* of the seeing-convolved flux profile for which we do not desire to make any aperture corrections and must therefore separate the aperture loss factor from the system response loss factor.

To achieve this goal, we allocate a set of 12 seven-fiber mini-IFU bundles to standard stars on every plate (six per spectrograph). Using the guider system to provide a first-order estimate for the seeing profile in a given exposure, we construct a model PSF as seen by each IFU minibundle by including the effects of wavelength-dependent seeing and the shape

mismatch between the focal plane and the plate. This allows us to estimate the relative fluxes among the seven IFU fibers in several wavelength windows and fit for the spatial location of the star within the IFU, the scale of the PSF, and the scale and rotation of the expected differential atmosphere refraction (see Section 8.1). With the best-fit PSF model, we can compute the aperture loss factor of the fibers and estimate the total flux that would have been observed for each standard star if the IFU had captured 100% of its light.

Given this aperture correction, we can then derive the system response as a function of wavelength in a similar way as BOSS (Dawson et al. 2013) by selecting the best-fitting template from a grid of theoretical spectra normalized to the observed SDSS broadband magnitudes. The correction vectors derived from the individual standard stars in a given exposure are then averaged to obtain the best system throughput correction to apply to all of the science fibers. This process is described in detail by Yan et al. (2016a).

The flux calibration vectors are derived on a per-exposure, per-camera basis, and hence result in four FITS files in which the sky-subtracted RSS have been divided by the appropriate flux calibration vector. These mgFFrame files (Table 8), are identical in format to the mgFrame and mgSFrame files, but have radiometric units of $10^{-17} \text{ erg s}^{-1} \text{ cm}^{-2} \text{ \AA}^{-1} \text{ fiber}^{-1}$ (see Appendix B). The accuracy of the MaNGA flux calibration has been described in detail by Yan et al. (2016a). In brief, we find that MaNGA’s relative calibration is accurate to 1.7% between the wavelengths of H β and H α and 4.7% between [O II] λ 3727 to [N II] λ 6584, and that the absolute rms calibration (based on independent measurements of the calibration vector) is better than 5% for more than 89% of MaNGA’s wavelength range. Yan et al. (2016a) assessed the systematic error by comparing the derived MaNGA photometry against PSF-matched SDSS broadband imaging, and found a median flux scaling factor of 0.98 in g -band with a sigma of 0.04 between individual galaxies. Since publication of the Yan et al. (2016a) study, additional improvements to the DR13 DRP that better model flux in the outer wings of the SDSS 2.5 m telescope PSF have improved the median flux scaling factor in g -band to 1.01 (see discussion by R. Yan et al. 2016b).

7. WAVELENGTH RECTIFICATION

The final step in the 2D section of the MANGADRP pipeline is to combine the four flux-calibrated frames into a single frame that incorporates all 1423 fibers from both spectrographs and combines together individual fiber spectra across the dichroic break at ~ 6000 Å onto a common fixed wavelength grid.⁴⁴ Although this introduces slight covariance into the spectra (and degrades the effective spectral resolution by $\sim 6\%$; see Section 10.2), it is required in order to ultimately coadd the individual spectra (each of which has its own unique wavelength solution) into a single composite 3D data cube. This rectification is achieved on a per-fiber basis by means of a cubic b-spline technique similar to that used previously in Section 5, but with a fixed breakpoint spacing of 1.21×10^{-4} in units of logarithmic angstroms (see Figure 14). In order to mitigate the impact of biases in the data-derived variances on the mean of the resulting spline fit (especially the dichroic overlap region) we weight the data with a version of the inverse

⁴⁴ The native CCD wavelength grid varies from fiber to fiber, but is ~ 1.0 Å pixel⁻¹ in the blue camera and ~ 1.4 Å pixel⁻¹ in the red camera.

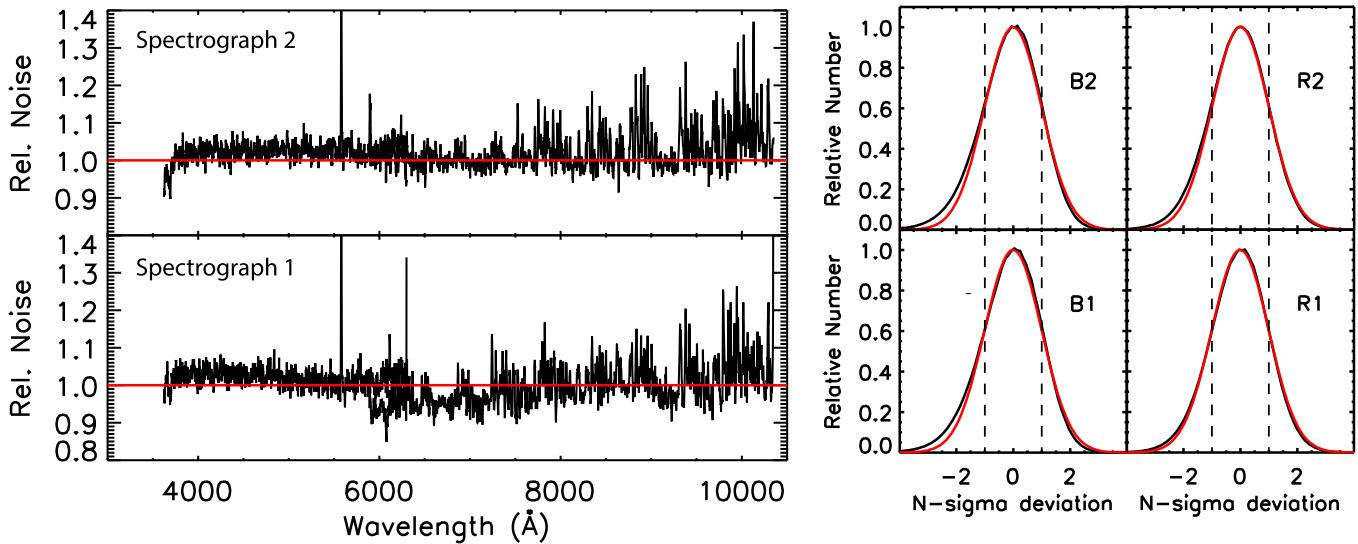


Figure 11. Left-hand panel: actual noise in sky-subtracted spectra (from all-sky plate 8069, observed on MJD 56901) divided by that expected based on detector read noise and Poisson counting statistics as a function of wavelength for each spectrograph. The overlapping region from $\lambda\lambda 5900\text{--}6300\text{ \AA}$ is the dichroic region over which blue and red cameras are combined. The solid red line indicates unity; if sky subtraction was done perfectly (and the noise properties of the spectra were estimated correctly) the black lines should nearly follow the red line at all wavelengths. Right-hand panel: distribution of noise values divided by the expected for all four cameras (B1/B2/R1/R2). Black curves represent the measured distribution of values ($3621\text{--}6300\text{ \AA}$ for B1 and B2, $5900\text{--}10354\text{ \AA}$ for R1 and R2), red curves represent the Gaussian ideal distribution with width $N\sigma = 1$. Vertical dashed black lines represent the 1σ range.

variance that has been smoothed with a five-pixel boxcar; weights for the blue camera are set to zero above 6300 \AA and weights for the red camera are set to zero below 5900 \AA .

We evaluate this bspline fit on two different fixed wavelength solutions, a decadal logarithmic and a linear. The logarithmic wavelength grid runs from 3.5589 to 4.0151 (in units of logarithmic angstroms) with a stepsize of 10^{-4} dex (i.e., 4563 spectral elements). This corresponds to a wavelength range of $3621.5960\text{--}10353.805\text{ \AA}$ with a dispersion ranging from $0.834\text{ \AA channel}^{-1}$ to $2.384\text{ \AA channel}^{-1}$, respectively. The linear wavelength grid runs from 3622.0 to 10353.0 \AA with a stepsize of $1.0\text{ \AA channel}^{-1}$ (i.e., 6732 spectral elements). These endpoints are chosen such that the resulting spectra come from regions of the BOSS spectrographs where the throughput is sufficiently high for practical faint-galaxy science purposes.

Finally, we perform a second-pass cosmic-ray identification on these camera-combined images by “growing” the previous cosmic-ray mask in both the fiberid and wavelength directions. Pixels within a one-pixel radius are included in the second-pass cosmic-ray mask if their flux is more than 5σ away from the sigma-clipped mean for a given fiber within a 50 pixel box in wavelength. This additional step significantly reduces the occurrence of unflagged cosmic-ray features in the final data products while only minimally ($\sim 2\%$) increasing the total number of flagged pixels.

The final flux-calibrated, camera-combined frames are saved as mgCFrame files (Table 9).

8. ASTROMETRIC REGISTRATION

Once a sufficient number of exposures has been obtained on a given plate that the cumulative S/N^2 of all complete sets exceeds the target threshold (see Section 2.2), it is marked as complete in the observing database and an “apocomplete” file is created in the MANGACORE repository that contains a list of all corresponding exposure numbers. This file serves as the trigger indicating that the DRP at the University of Utah should

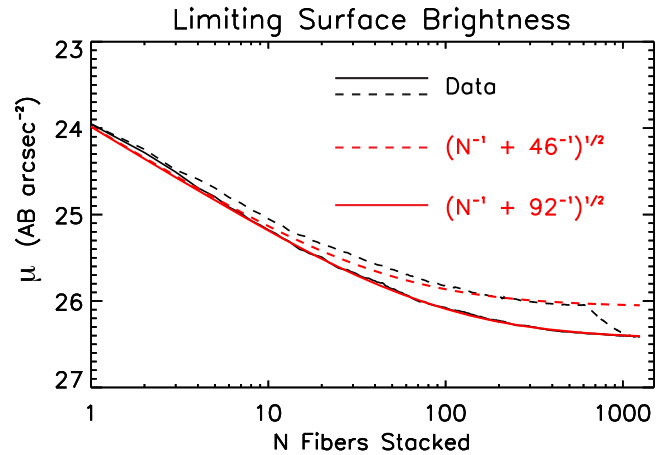


Figure 12. 1σ limiting surface brightness reached in the wavelength range $\lambda\lambda 4000\text{--}5500\text{ \AA}$ in a single 15 minute exposure by a composite spectrum stacking N sky-subtracted science fibers (based on all-sky plate 8069, observed on MJD 56901). The solid black line indicates results from stacking N science fibers selected randomly from across both spectrographs; this is extremely well reproduced by the theoretical curve (solid red line) representing expected performance based on $\sqrt{N^{-1} + 92^{-1}}$. The dashed black line indicates results from stacking N science fibers as a function of fiberid along the spectrograph slit; this improves more slowly at first as $\sqrt{N^{-1} + 46^{-1}}$ (red dashed line).

enter the 3D stage of processing and combine together individual exposures into final-form data cubes and RSS for each IFU on the plate.

Using the metadata archived in MANGACORE, spectra for each IFU target are pulled from the corresponding lines of the mgCFrame files and collated into a single RSS file containing all of the spectra associated with a given object (manga-RSS; see Table 10 and discussion in Appendix B.2). Typically, this corresponds to $3 \times N_{\text{set}} \times N_{\text{ifu}}$ spectra, where N_{set} is the number of complete sets of exposures observed, and N_{ifu} is the

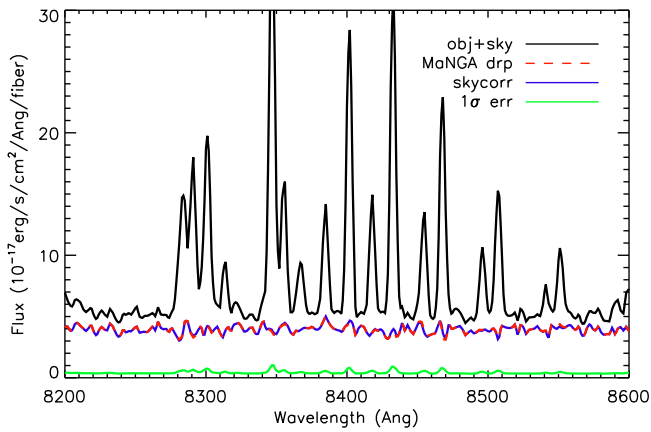


Figure 13. Example spectrum of a randomly chosen MaNGA fiber from a typical galaxy plate (plate 7443, MJD 56745, exposure 177685) in the vicinity of an OH airglow region. The black line represents the as-observed galaxy + sky spectrum, the dashed red line the science spectrum after sky subtraction using the MaNGA DRP, and the blue line the science spectrum using instead the skycorr (Noll et al. 2014) algorithm. The two methods of sky subtraction produce nearly identical results to within the DRP-estimate uncertainty (green line).

number of fibers in the IFU. After resorting the input spectra into a row-stacked format on a per-galaxy basis the DRP calculates the astrometric solution for each of the fibers. This astrometric calibration has two stages: a basic module that computes fiber locations based on reference metadata and theoretical refraction models, and an advanced module that fine-tunes the zeropoint location and rotation of the basic solution by registering the spectra against SDSS broadband photometry.

8.1. Basic Astrometry Module

The effective location of a particular IFU fiber in any given exposure is dictated by numerous optomechanical factors. Many of these are possible to either measure or estimate for an arbitrary source, and the MaNGA basic astrometry module combines these factors into a single wavelength-dependent position vector (in R.A./decl.) for each fiber. These factors include the following.

1. Relative and absolute fiber location within a given IFU ferrule based on the as-built fiber bundle metrology. This is measured during the manufacturing process to a typical accuracy $\sim 0.3 \mu\text{m}$ (relative)⁴⁵ and $\sim 5 \mu\text{m}$ (absolute; see Drory et al. 2015) and recorded in MANGACORE for each harness serial number.
2. Offset of an IFU from its base position due to the three-point dithering pattern. We assume that the dithering exactly matches the commanded offsets; the accuracy of this assumption is limited by the ~ 0.1 arcsec dithering accuracy of the telescope (see Law et al. 2015).
3. Offset of drilled holes from the intended drilling location. Although holes can be drilled to within an accuracy of $\sim 9 \mu\text{m}$ rms, they are measured after the fact to an accuracy $\sim 5 \mu\text{m}$. This information is recorded for each plate in MANGACORE.
4. Chromatic DAR relative to the guide wavelength ($\sim 5500 \text{ \AA}$). This shifts the effective location of each

fiber as a function of wavelength (i.e., a given fiber receives light from a different part of a target galaxy at blue versus red wavelengths). The magnitude and direction of this effect is calculated using the SDSS plate design code model (based in part on Filippenko 1982) as discussed in detail by Law et al. (2015) and depends on the altitude, the parallactic angle, and the atmospheric temperature/pressure/humidity. We calculate the expected effect at the midpoint of a given exposure for each of the 4563 wavelength channels (for the logarithmic case) given the known location of each IFU on the sky and atmospheric conditions recorded in the headers of individual exposures.

5. Global shift of the IFU location at the guide wavelength due to field DAR. Over the 3° field of an SDSS plate there are changes in scale and rotation of the sky image (in particular, altitude-dependent compression along the altitude axis). The telescope guiding software corrects for these effects averaged over the plate, but cannot fully correct the quadrupole distortion in the effective location of a given IFU. We estimate this effect as discussed in detail by Law et al. (2015).
6. Wavelength-dependent distortions due to the SDSS telescope optics. These are estimated based on upon optical models of the telescope in the SDSS plate design code (Gunn et al. 2006).

The final product of the basic astrometry module is a pair of two-dimensional arrays (matched in size to the mgCFrame flux array) that give the X and Y fiber positions (in units of arcseconds in the tangent plane) relative to the nominal IFU center IFURA, IFUDEC. These arrays can thereafter be used to look up the effective on-sky location corresponding to any wavelength, for any fiber.

8.2. Extended Astrometry Module

During operations within a single dark run a MaNGA cartridge will remain plugged with a given plate until observations for that plate are complete. Since MaNGA shares carts with APOGEE-2 N, however, at the end of a dark run it is typically necessary to unplug the MaNGA IFUs from unfinished plates and replug them again the following dark run to continue observations. This replugging introduces an uncertainty into the relative centering and rotation of each IFU in its hole at the level of ~ 0.5 arcsec (centering) and $\sim 2^\circ$ – 3° (rotation) from the required clearance of locator pins within their holes. The precise change cannot be measured directly and will change from plugging to plugging as it depends on the torsional stresses arising from the routing of each IFU cable through a cartridge. Such uncertainties⁴⁶ are significantly larger than any of the uncertainties derived from effects described in Section 8.1.

We therefore follow the method employed by the VENGA survey (Blanc et al. 2013) of registering the fiber spectra from each exposure against SDSS broadband imaging. In this “extended astrometry module” (EAM) we compute the synthetic broadband flux of each fiber by integrating the flux-calibrated spectrum over the corresponding transmission curve. We then search a grid in right ascension, declination, and rotation of the fiber bundle relative to the base position

⁴⁵ $0.3 \mu\text{m}$ corresponds to 5 mas at the SDSS focal plane ($\sim 60 \mu\text{m arcsec}^{-1}$).

⁴⁶ At the outer ring of a 127 fiber IFU such a 3° rotational uncertainty corresponds to ~ 0.8 arcsec.

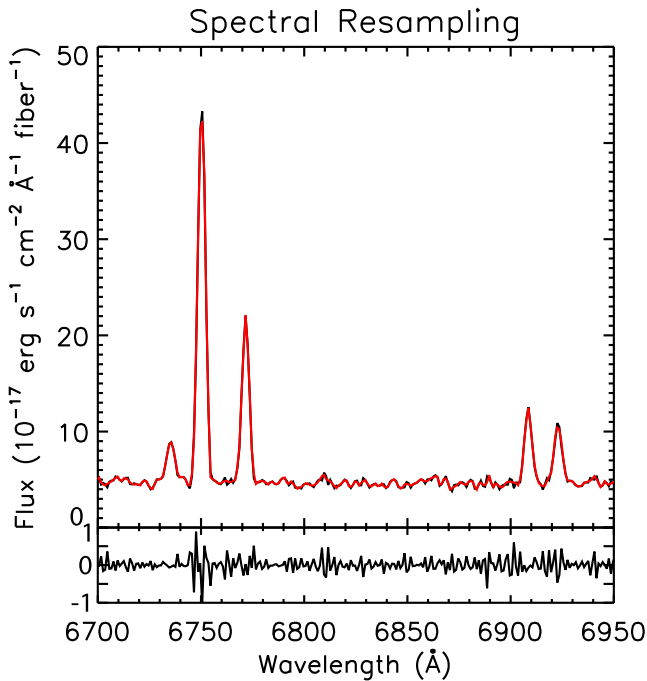


Figure 14. Example MaNGA spectrum in the vicinity of $H\alpha$, $[N II]$, and $[S II]$ emission on the native CCD pixel scale (solid black line) overlaid with the cubic bspline fit evaluated on a constant logarithmic wavelength grid (solid red line). The lower panel shows the difference between the native spectrum and the wavelength-rectified spline fit.

determined in Section 8.1 (we keep the relative positions of fibers within the bundle fixed). At each position on the grid the fiber coordinates (collapsed from the basic astrometry solution over the appropriate wavelength range) are shifted accordingly, and aperture photometry is performed on a PSF-matched SDSS broadband image using 2.0 arcsec diameter apertures for each fiber. An additional overall flux normalization is permitted according to

$$f_{SDSS} = A f_{MaNGA} + B \quad (1)$$

where f_{SDSS} and f_{MaNGA} are the SDSS broadband and MaNGA fiber fluxes, respectively, A is a multiplicative scaling factor, and B represent a zeropoint shift.⁴⁷ Yan et al. (2016a) presented a discussion of these A and B coefficients, and determined that A had a roughly Gaussian distribution centered about 1.00 (in i -band) with a sigma of 0.037 for $\sim 25,000$ IFU-exposures obtained during the first year of operations, indicating that the spectrophotometric accuracy of the MaNGA data is about 4% with respect to the SDSS imaging data. The best-fit values of position, rotation, and flux offsets are determined via χ^2 minimization, with corresponding uncertainties drawn from the χ^2 probability maps. This exercise is repeated in each of the four g , r , i , and z bands, with the final result a biweight mean of the four bands (this provides robustness against occasional unmasked cosmic rays).

⁴⁷ We note that these A and B terms are derived for informational purposes only; we do not apply corrections from them to the data but rather use them as an independent check on the flux calibration of each frame and flag exposures as problematic where A or B deviate substantially from 1.0 and 0.0, respectively.

Unsurprisingly, the EAM can achieve better results for larger fiber bundles on galaxies with significant azimuthal structure than for smaller bundles on smooth and circular galaxies. In Figure 15 we show EAM results for two commissioning galaxies 7443–12703 and 7443–3702. For the large IFU on a source with significant structure (7443–12703) the measurement uncertainties on both positional shift and global rotation are small, and reveal (in this case) a ~ 0.5 arcsec shift in the IFU center across a cartridge replugging. In contrast, for the small IFU on a rotationally symmetric source (7443–3702) the positional shift is still well constrained but the global rotation is almost completely unconstrained in the range of values explored by the EAM ($\pm 5^\circ$).

In order to avoid introducing errors into our astrometry due to such noisy measurements, we therefore run the EAM iteratively. In the first pass, each exposure is fitted independently. The derived values of $\Delta\theta$ are then averaged across all exposures in a given plugging, and the EAM run again holding $\Delta\theta$ fixed at these average values in order to better determine positional shifts between exposures. Since rotation is expected to change only between repluggings (consistent with observed behavior based on galaxies with sufficient azimuthal structure to measure $\Delta\theta$ reliably), this allows us to mitigate the uncertainty in any individual measurement of bundle rotation. In contrast, such averaging is not justified for the positional shifts. Although such shifts are dominated by repluggings (e.g., Figure 15), smaller shifts at the ~ 0.1 arcsec level are possible due to uncertainties in the applied dither offsets that we wish to correct through the EAM. On average, we find that the median astrometric uncertainty of the exposures making up the 1390 galaxies in DR13 relative to the SDSS preimaging data is ~ 0.1 arcsec (1σ) based on the reduced χ^2 surface.

Since each set of three exposures is known to have uniform coverage (see Law et al. 2015; R. Yan et al. 2016b) sets from different pluggings of a given plate (and indeed, even between different cartridges) can therefore be combined together onto a common astrometric solution using the EAM. Since all MaNGA target galaxies are drawn from the SDSS imaging footprint, this correction is automatically applied to all MaNGA galaxies.⁴⁸

9. DATA CUBE CONSTRUCTION

9.1. Basic Cube Building

Using the RSS files and associated astrometric solutions derived in Section 8 we combine the individual fiber spectra into rectilinearly gridded cubes (with orientation R.A., decl., λ) for each IFU on both logarithmic and linearly sampled wavelength solutions. Since these input spectra have already been resampled onto a common wavelength grid, this simplifies to the two-dimensional reconstruction of a regularly gridded image from an irregularly sampled cloud of measurements of the intensity profile at a given wavelength channel.

Multiple methods exist for performing such image reconstruction (see Section 9.2); we choose to build our data cubes one image slice at a time using a flux-conserving variant of Shepard’s method similar to that used by the CALIFA pipeline (Sánchez et al. 2012). At each of the 4563 wavelength channels

⁴⁸ The method will fail on point-like sources and some ancillary targets outside the SDSS imaging footprint; for these objects the EAM is disabled and the basic astrometry module is used alone.

(for the logarithmically sampled data; 6732 for the linear), we describe our input data as one-dimensional vectors of intensity $f[i]$ and variance $g[i]$ with length $N = N_{\text{fiber}} \times N_{\text{exp}}$ where N_{fiber} is the number of fibers in the IFU (e.g., 127) and N_{exp} is the total number of exposures to combine together. Similarly, we can construct vectors x and y , which describe the effective position of the center of each fiber based on the astrometric solution derived in Section 8, and converting to fractional pixel coordinates relative to some chosen origin and pixel scale. We adopt a spatial pixel scale of $0.5 \text{ arcsec pixel}^{-1}$ and an output grid of size X_{max} by Y_{max} taken to be slightly larger than the dithered footprint of the MaNGA IFU.

Each of the $M = X_{\text{max}} \times Y_{\text{max}}$ pixels in the output image can likewise be resorted into a one-dimensional array of values, with the pixel locations given by $X[j]$ and $Y[j]$, respectively, for $j = 1$ to M . The mapping between the $f[i]$ intensity measurements in the irregularly sampled input and the $F[j]$ intensities in the regularly sampled output image are then determined by the weights $w[i, j]$ describing the relative contribution of each input point to each output pixel. We take this weight function to be a circular Gaussian:

$$w[i, j] = b[i] \exp\left(-0.5 \frac{r[i, j]^2}{\sigma^2}\right) \quad (2)$$

where $\sigma = 0.7 \text{ arcsec}$ is an exponential scale length, $r[i, j] = \sqrt{(x[i] - X[j])^2 + (y[i] - Y[j])^2}$ is the distance between the i 'th fiber location and the j 'th output grid square, and $b[i]$ is a binary integer equal to zero where the inverse variance $g[i]^{-1} = 0$ and one elsewhere. Essentially, $b[i]$ functions as a mask that allows us to exclude known bad values in individual spectra from the final combined image. Additionally, we set $w[i, j] = 0$ for all $r[i, j] > r_{\text{lim}} = 1.6 \text{ arcsec}$ as an upper limit on the radius of influence of any given measurement. These limiting radii and scale lengths are chosen empirically based on observed performance; the present values are found to provide the smallest reconstructed FWHM for stellar targets observed as part of commissioning (see Section 10.1) while not introducing spurious structures by shrinking the impact-radius of individual fibers too severely.

In order to conserve flux we must normalize the weights such that the sum of the weights contributing to any given output pixel is unity. The normalized weight function is therefore

$$W[i, j] = \frac{w[i, j]}{\sum_{i=1}^N w[i, j]} \quad (3)$$

where in order to avoid divide by zero errors we set $W[i, j] = 0$ where $w[i, j] = 0$ for all i in the range 1 to N (e.g., outside the hexagonal footprint of the IFU).

The intensity distribution of the pixels in the output image may therefore be written as the matrix product of the normalized weights and the input intensity vector:

$$F = \alpha W \times f = \alpha \begin{bmatrix} W_{11} & \dots & W_{N1} \\ \vdots & \ddots & \vdots \\ W_{1M} & \dots & W_{NM} \end{bmatrix} \times \begin{bmatrix} f_1 \\ \vdots \\ f_N \end{bmatrix} \quad (4)$$

or alternatively as

$$F[j] = \alpha \sum_{i=1}^N f[i] W[i, j] \quad (5)$$

where $\alpha = 1/(4\pi)$ is a constant factor to account for the conversion from flux per unit fiber area ($\pi \text{ arcsec}^2$) to flux per unit spaxel area (0.25 arcsec^2). The resulting $F[j]$ may then trivially be rearranged to form the output image at this wavelength slice given the known mapping of the pixel coordinates $X[j]$ and $Y[j]$.

Similarly, the variance G of the rectified output image may be written as

$$G[j] = \alpha^2 \sum_{i=1}^N g[i] (W[i, j])^2. \quad (6)$$

This calculation therefore propagates the uncertainties in individual spectra through to the final data cube, but does not use these uncertainties in constructing the combined flux values (except for the simple masking of bad values where inverse variance is equal to zero).

These rectified images of the intensity profile and the corresponding inverse variance maps at each wavelength channel are reassembled by the DRP into three-dimensional cubes along with a 3D quality mask describing the effective coverage and data quality of each spaxel. The final MANGA-CUBE files are discussed further in Appendix B.2 (see also Table 11).

9.2. Algorithm Choice

As stated in Section 9.1, there are multiple algorithms that we could have adopted for building our data cubes, ranging from surface-fitting techniques (e.g., thin plate spline fits) to drizzling and our adopted modified Shepard approach. Based on idealized numerical simulations performed prior to the start of the survey, we found that the surface-fitting approach provided reasonable quality reconstructed images, but was nonetheless undesirable because there is no simple means by which to propagate uncertainties in the resulting surface. In contrast, the modified Shepard approach allows for easy calculation of both the variance and covariance of the reconstructed data cubes, as described in Section 9.3.

The drizzle approach (Fruchter & Hook 2002) has been tested by ourselves and by the CALIFA (Sánchez et al. 2012) and SAMI (Sharp et al. 2015) surveys, all of whom have found that (1) it broadened the final PSF, and (2) since fiber bundle IFUs have $<100\%$ fill factor in a given exposure it can create artificial structures in the intensity distribution following the footprint of the circular fibers. To mitigate this problem the SAMI survey (see discussion by Sharp et al. 2015) adopted a weighting system based on the ratio between the original fiber area and the area covered by a final spaxel of a particular fiber (if the fiber is reduced by an arbitrary amount smaller than the original size). This in essence redistributes the flux following a weighting that depends on the distance to the centroid of the fiber and is truncated at a maximum distance controlled by the arbitrary reduction of the covered area of the fibers. This weighting function results in sharper images, but in order to smooth out the artificial structure in the intensity distribution (Sharp et al. 2015, see their Figures 7 and 9) found that a large

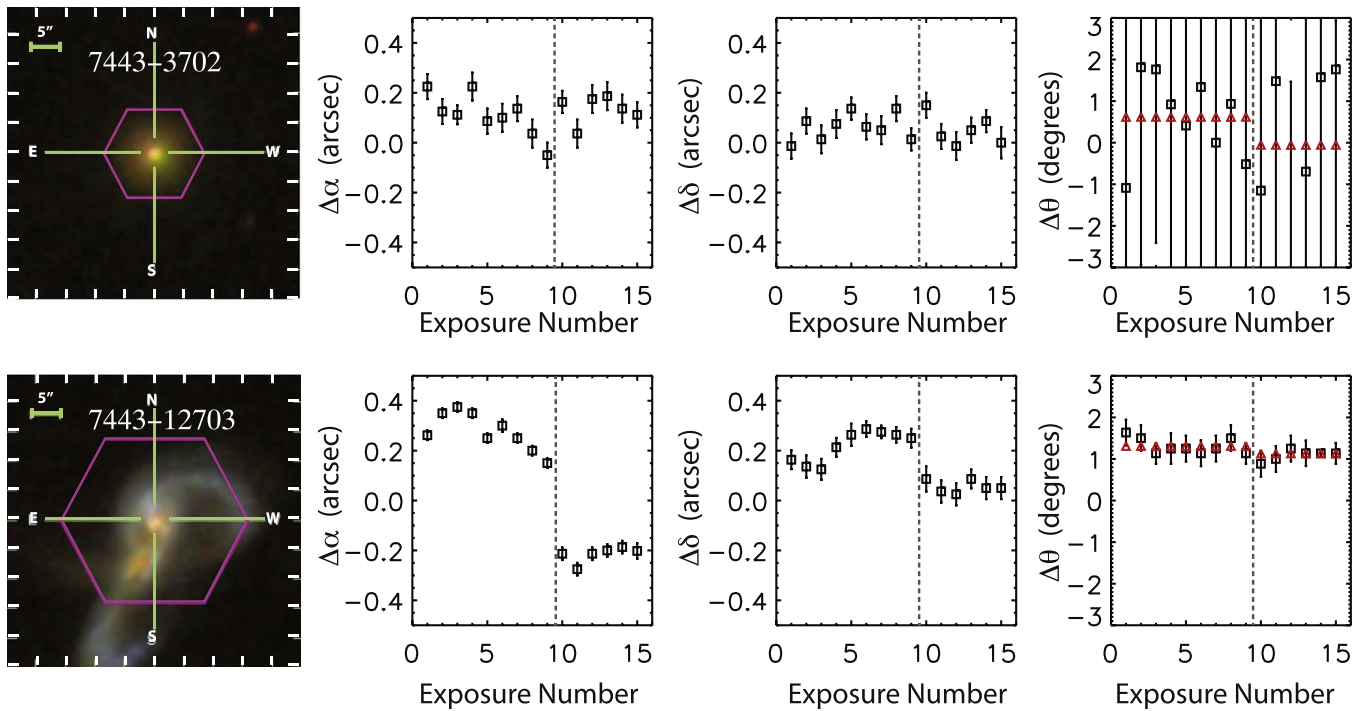


Figure 15. MaNGA EAM performance for two commissioning galaxies 7443–12703 and 7443–3702 (mangaid 12-193481 and 12-84670, respectively). The leftmost panel shows a three-color image of each galaxy based on SDSS imaging data, overlaid with a hexagonal bounding box indicating the footprint of the MaNGA IFU. The remaining boxes show the values calculated by the EAM for the relative shift in right ascension, declination, and bundle rotation between exposures (open black boxes with associated 1σ uncertainties). Red boxes in the right-hand panel show the average values in $\Delta\theta$ adopted for all exposures in a given plugging in a second run of the EAM. Values shown for the shifts $\Delta\alpha$ and $\Delta\delta$ are after this second-pass with fixed $\Delta\theta$. The vertical dotted line represents a replugging of the plate between exposures 9 and 10.

number of dither positions (≥ 7) was required to sufficiently sample the galaxy.

Such an approach is not viable for MaNGA (or CALIFA) for a variety of reasons. First, the effective filling factor of the MaNGA IFUs is lower than that of SAMI (56% versus 75%; see Law et al. 2015), meaning the gaps in coverage for a given exposure are larger (although much more regular). Second, the inner diameter of the MaNGA fibers (2 arcsec) and the fiber-to-fiber spacing in the IFUs (2.5 arcsec) is large compared to the typical FWHM of the observational seeing (~ 1.5 arcsec), meaning that the spatial resolution incident upon the IFU bundles is drastically undersampled in a single exposure. Most importantly, however, the MaNGA survey strategy of reaching constant depth on each target field requires a different total number of exposures depending on observational conditions and the Galactic foreground extinction. The number of exposures on a given target can therefore range from 6 to 21, obtained in sets of three dithered exposures that must achieve uniform coverage and good reconstructed image quality. Similarly, the SAMI approach also does not work for CALIFA since CALIFA often has only a single visit to a given field.

In contrast, the modified Shepard approach adopted in Section 9.1 allows for high-quality image reconstruction from just three dithered exposures that can be repeated as necessary to achieve the desired depth in a given field (see discussion in Law et al. 2015). This algorithm was found to perform well based on prior experience with the CALIFA survey, and in numerical simulations designed to optimize the choice of the scale length and truncation radius for the exponential weighting function. We note that although the MaNGA and SAMI approaches to cube building are *conceptually* different they are

mathematically quite similar, albeit that the SAMI weighting function does not follow a Gaussian distribution and the kernel is in essence sharper (i.e., with smaller size and truncation radius).

9.3. Covariance

The redistribution of intensity measurements from individual fibers into a rectilinearly sampled data cube via the equations in Section 9.1 leads to significant covariance among spatially adjacent pixels at each wavelength slice. The formal covariance matrix of each slice of the data cube can be written via matrix multiplication as

$$C = \alpha^2 W \times (g' \times W^T) \quad (7)$$

where α is again a constant scale factor, and g' is the diagonal variance matrix

$$g' = \begin{bmatrix} g_1 & 0 & \dots & 0 \\ 0 & g_2 & \dots & 0 \\ \vdots & \vdots & \ddots & \vdots \\ 0 & 0 & \dots & g_N \end{bmatrix}. \quad (8)$$

The diagonal elements of C represent the M elements of the variance array $G[j]$ for the output image while the off-diagonal elements of C represent the covariance introduced between different pixels in the output image by the chosen weighting method. These may in turn be recast as the correlation matrix ρ , where $\rho_{jk} = C_{jk} / \sqrt{C_{jj}C_{kk}}$ for all j and k from 1 to M . ρ is thus unity along the diagonal elements (since each pixel has unity correlation with itself). Following this exercise, we find that,

generally, pixels separated by $0''.5$ (1 pixel) have correlation coefficients of $\rho \approx 0.85$, decreasing to $\rho < 0.1$ (i.e., nearly uncorrelated) at separations of ≥ 2 arcsec. Spatial covariance therefore becomes important when, for example, one calculates the inverse variance in a spectrum generated by coadding many adjacent spaxels.

Although ρ is nominally a large matrix, in practice it is both symmetric and sparse, containing mostly zero-valued elements since we have truncated the weight function to be zero outside a radius of 1.6 arcsec. Since the MaNGA reconstructed PSF is only a weak function of wavelength, ρ also changes only slowly with wavelength, meaning that values of ρ at a given wavelength may generally be interpolated from adjacent wavelengths. In a future data release, the DRP will therefore include the correlation matrix at the central wavelengths of the *griz* bands in the final data products of the cube building algorithm. At the present time in DR13, however, these correlation matrices are not yet available, and we therefore provide a rough calibration of the typical covariance in the MaNGA data cubes following the conventions established by the CALIFA survey (Husemann et al. 2013). Specifically, we provide a calibration of the nominal calculation of the noise vector of a coadded spectrum under the incorrect assumption of no covariance to one determined from a rigorous calculation that includes covariance.

We have done so using an idealized experiment. Using five data cubes from plate 7495, one of each of the fiber-bundle sizes, we synthetically replace each RSS spectrum with unity flux and Gaussian error. We then construct the data cube identically as done for our galaxy observations. We bin the resulting spaxels using a simple boxcar of size N^2 where $N = 1, 3, 5, 7,$ and 9 , and calculate the mean and standard deviation in the resulting spectrum. This noise estimate is our *measured* error, n_{measured} . Alternatively, we can use the inverse-variance vectors for each spaxel in the synthetic data cube that results from the nominal calculation above to create a separate noise estimate, which instead assumes that each spaxel is independent. This calculation follows nominal error propagation, but does not account for the covariance between spaxels; we refer to this as $n_{\text{no covar}}$. The ratio of these two estimates is shown in Figure 16.

Figure 16 demonstrates that the true error in a combined spectrum is substantially larger than an error calculated by ignoring spatial covariance. The relationship of the errors with and without covariance depends upon the number N_{bin} of spaxels combined. For small N_{bin} the values in nearby spaxels are highly correlated and the S/N is nearly constant with N_{bin} (i.e., both the signal and the true error increase proportionally to N_{bin}). At large N_{bin} the values in combined spaxels are nearly uncorrelated, and the S/N increases proportionally to $\sqrt{N_{\text{bin}}}$.

We have thus fit a functional form identical to that used by Husemann et al. (2013) to our measurements in Figure 16 and find that

$$n_{\text{measured}}/n_{\text{no covar}} \approx 1 + 1.62 \log(N_{\text{bin}}), \quad (9)$$

for $N_{\text{bin}} \lesssim 100$, and

$$n_{\text{measured}}/n_{\text{no covar}} \approx 4.2 \quad (10)$$

for $N_{\text{bin}} > 100$ (i.e., beyond ~ 2 times the FWHM where spaxels are uncorrelated).

It is important to note that the binned spaxels must be adjacent for this calibration to hold; i.e., a random selection of

spaxels across the face of the IFU will not show as significant an effect because they will not be as strongly covariant. The inset histogram shows the ratio of the data to the fitted model in Equation (9), demonstrating the calibration is good to about 30%. We have confirmed this result empirically by comparing the standard deviation of the residuals of the best-fitting continuum model for a large set of galaxy spectra, following an approach similar to Husemann et al. (2013). However, we emphasize that the test we have performed to produce Figure 16 is more idealized and controlled. We also confirm that a rigorous calculation of the covariance, following the matrix multiplication discussed at the beginning of this section, and a subsequent calculation of the noise vector in the binned spectra used in Figure 16 are fully consistent with our measurements n_{measured} .

10. DATA QUALITY

10.1. Data Cubes: Angular Resolution

An estimate of the spatial light profile of an unresolved point source (i.e., the “reconstructed PSF”) is automatically provided for each data cube using a numerical simulation tied to the specific observing conditions of each exposure. Using the known fiber locations for a given exposure, the DRP computes the flux expected to be recorded by each fiber from an unresolved point source located at the center of the IFU. This model flux is based on integration of the nominal PSF incident on the face of the IFU in the focal plane of the SDSS 2.5 m telescope. The focal-plane PSF is taken to be a double-Gaussian that accounts for chromatic distortions due to the telescope optics and observational seeing recorded by the guide camera. As detailed by Yan et al. (2016a), since the guide camera reports image FWHM systematically larger than measured by the MaNGA IFU fiber bundles, the guider seeing measurements are also “shrunk” by a scale factor determined by the flux calibration module to give an incident PSF that best matches differential fiber fluxes recorded by the 12 photometric standard star mini-bundles. These simulated fiber fluxes are reconstructed into a data cube using the same algorithm as the science data, and slices of this cube corresponding to *g*, *r*, *i*, and *z* bands are attached to each data cube.

These *griz* images (GPSF, RPSF, IPSF, ZPSF; see Appendix B.2) provide a reasonable estimate of the reconstructed PSF in each data cube and are reported in each of the FITS headers. We confirmed the fidelity of these reconstructed PSF models by observing a plate during survey commissioning in which every MaNGA IFU targeted bright stars with two sets of dithered observations (i.e., following the methodology of typical galaxy observations). This plate (7444) was processed by the DRP in an identical manner to standard galaxy plates, with the exception that only the basic astrometry module was used to register the fiber locations since there is no extended structure against which to use extended astrometry module.

In Figure 17 we show the profiles of stars in four of the reconstructed data cubes compared to the simulated estimates. We find that the actual reconstructed PSF of these data cubes is well described by a single 2D Gaussian function with normalized intensity

$$I(r) = \frac{1}{2\pi\sigma^2} \exp(-r^2/2\sigma^2) \quad (11)$$

where 2.35σ is the standard Gaussian FWHM. This profile is well matched to the model PSF estimated based on mock integrations of an artificial point source at the known fiber positions; the model FWHM estimates agree with the measured values to within 1%–2%. The measured FWHM of the reconstructed PSF for the other 13 IFUs on plate 7444 similarly lie in the range 2.4–2.5 arcsec.⁴⁹ Based on the simulations presented by Law et al. (2015) and the range of Ω uniformity values for DR13 reported by R. Yan et al. (2016b) we expect that the reconstructed PSF FWHM should vary by less than 10% across a given IFU.

As discussed in greater detail by R. Yan et al. (2016b), the range of *g*-band reconstructed PSF FWHM in the 1390 DR13 galaxy data cubes is generally distributed in the range 2.2–2.7 arcsec, with a tail to about 3 arcsec (Figure 17).

10.2. Data Cubes: Spectral Resolution

As indicated in Section 4.2.5, the LSF varies along the spectrograph slit, and hence varies spatially within a given IFU. Similarly, the LSF can also vary between exposures with ambient temperature drifts and changes in the focus of the spectrograph. The typical spectral resolution for DR13 galaxies is shown in Figure 18; typical IFUs show rms variability at the level of 1%–2% (blue shaded region), while the worst-case large IFUs on the ends of the spectrograph slit can show variability as high as 8%–10% at blue wavelengths (red shaded region). This variability within the worst-case IFUs is dominated by the along-slit variability, but compounded by variations between exposures. The focus in the red cameras is significantly flatter than in the blue cameras, meaning that variation in spectral resolution longward of 6000 Å is 1% or less even for the worst-case IFUs.⁵⁰

Each MaNGA data cube therefore has an associated extension (see Appendix B.2) describing both the mean and 1σ deviation about the mean spectral resolution for all fiber spectra contributing to the cube. Detailed information on spectral resolution of the individual fiber spectra used to create a given data cube are contained in the final RSS files.

After finalization of the DR13 data pipeline it was realized that the instrumental LSF estimates reported by the pipeline are systematically underestimated. There are two factors that contribute to this underestimation; first, the LSFs reported in DR13 correspond to native Gaussian widths prior to convolution with the boxcar detector pixel boundaries (i.e., the Gaussian function is integrated over the pixel boundaries), while many third-party analysis routines simply evaluate Gaussian models at the pixel midpoints. Although neither approach is necessarily more “correct” than the other, this nonetheless represents a systematic difference between the values quoted and the values that would be measured with most third-party routines. Second, the wavelength rectification performed in Section 7 effectively resamples the spectra and introduces a broadening into the LOG and LINEAR-format spectra that is not accounted for by the DR13 data pipeline. These issues are not unique to the MaNGA data and pipeline,

but rather affect all previous generations of SDSS optical fiber spectra as well.

Efforts to address this discrepancy are ongoing (see, e.g., K. Westfall et al., in preparation) and will be detailed in a future version of the MaNGA data pipeline. In the present contribution, we note that re-analysis of ~ 2500 individual exposures suggests that multiplying the DR13 LSF by a factor of 1.10 gives a reasonable first-order correction (i.e., the spectral resolution of the DR13 data products is overestimated by $\sim 10\%$). This correction factor accounts for both the pre- versus post-pixelization Gaussian difference ($\sim 4\%$) and the wavelength rectification broadening ($\sim 6\%$).

10.3. Wavelength Calibration

Based on previous calculations for the BOSS redshift survey (e.g., Bolton et al. 2012, their Figure 14), the MaNGA spectra (which share the same instrument and much of the same reduction pipeline software) should also have absolute wavelength calibration good to $\sim 5 \text{ km s}^{-1}$. We verify this estimate by comparing bright emission line features in the MaNGA data cubes against publicly available SDSS-I single-fiber spectra of each of the galaxies in DR13. For each galaxy, we obtain the corresponding SDSS-I spectrum from SkyServer,⁵¹ and determine the effective location of the spectrum from the PLUG_RA and PLUG_DEC header keywords. We then perform aperture photometry in a 2 arcsec circular radius about this location at every wavelength slice of the MaNGA data cube in order to construct a 1D MaNGA spectrum of the central pointing. Both the SDSS-I and MaNGA spectra are then fitted with single-Gaussian emission line components at the expected wavelengths of the H β , [O III] $\lambda 5007$, H α , and [N II] $\lambda 6583$ nebular emission lines given the known galaxy redshift from the NASA-Sloan Atlas (NSA; Blanton et al. 2011).⁵²

Although many of the MaNGA galaxies do not have strong emission line features in their central spectra, sufficiently many do in order to allow us to statistically compare the MaNGA and SDSS-I spectra. Considering only galaxies for which both MaNGA and SDSS fits are within 5 Å of the nominal wavelength, have σ width of 0.5–5 Å, and line fluxes $> 10^{-16} \text{ erg s}^{-1} \text{ cm}^{-2}$, we find that 470/670/760/1063 galaxies fulfill the criteria for H β , [O III], H α , and [N II], respectively. In Figure 19 we plot the distribution of relative peak velocity offsets for each of these four emission lines. We conclude that there is no systematic offset between the MaNGA and SDSS-I spectra to within $\sim 2 \text{ km s}^{-1}$, and that individual galaxies are distributed nearly according to a Gaussian with 1σ width $\sim 10 \text{ km s}^{-1}$.

This width may in part, however, reflect intrinsic velocity gradients within the galaxies combined with uncertainties at the few tenths of an arcsecond level in the effective location of the SDSS-I fibers due to hardware tolerances and DAR.⁵³ Using the MaNGA IFU spectra, we find that changes in location at the level of just 0.25 arcsec (compared to the typical MaNGA astrometric uncertainty of 0.1 arcsec; see Section 8.2) can easily result in $\sim 20 \text{ km s}^{-1}$ velocity shifts in the resulting spectra for galaxies with strong central velocity gradients (e.g., 8453–12703). The actual wavelength accuracy of the MaNGA

⁴⁹ Except for one 19-fiber IFU, for which the reconstructed image is clearly out of focus, indicating that it partially fell out of the plate. Such cases are rare, and detected during quality-control checks by the extended astrometry module.

⁵⁰ Except around 8100 Å where the red detectors have a two-phase discontinuity (see Section 4.2.5).

⁵¹ SkyServer is a web-based public interface to the SDSS archive; see <http://skyserver.sdss.org/dr12/en/home.aspx>.

⁵² <http://www.nsatlas.org>

⁵³ Indeed, the SDSS-I spectra also have effective locations that *change* as a function of wavelength due to chromatic atmospheric refraction.

spectra may therefore more accurately be given by the rms agreement between repeat MaNGA observations of a small sample of galaxies in DR13; indeed, although there are only ~ 10 repeat observations with strong emission lines in DR13, we find a typical rms agreement of 5 km s^{-1} between the four emission line wavelengths above.

The *relative* wavelength calibration accuracy of the individual fibers within a given IFU is more difficult to assess in the absence of a calibration reference. However, we can obtain a rough estimate by considering the rms scatter between the measured centroids of bright skylines and the fitted value adopted by the pipeline as described in Section 4.3. As a conservative estimate,⁵⁴ we assume that the smallest rms among the individual skyline measurements is indicative of the relative wavelength calibration accuracy. At 0.024 pixels at 8885 \AA , this suggests a relative fiber-to-fiber wavelength calibration accuracy of better than 1.2 km s^{-1} rms.

10.4. Typical Depth

Finally, we illustrate the overall quality of the MaNGA spectral data by comparing the spectrum of the central region of galaxy 7443–12704 (aka UGC 09873) from the MaNGA commissioning plate against previous SDSS-I single-fiber and CALIFA⁵⁵ DR-2 (Sánchez et al. 2012; Walcher et al. 2014; García-Benito et al. 2015) IFU observations of the same galaxy. Such a direct comparison is intrinsically difficult as the total flux in a given circular aperture is strongly affected by both the observational seeing and chromatic differential refraction (for SDSS-I) and by the effective spatial resolution of the reconstruction data cubes (MaNGA and CALIFA), especially in regions of the galaxy where there is a strong gradient in the intrinsic surface brightness (i.e., near the center). This method is therefore good for comparing the *relative* shapes of spectra from different surveys, but not the overall normalization of the flux calibration (which should instead be assessed through PSF-matched broadband imaging, e.g., Yan et al. 2016a).

In this case, the SDSS-I spectrum (observed in 2004 May, and obtained from the DR12 Science Archive Server) corresponds to a circular fiber with a core diameter of 3 arcsec observed in ~ 1.6 arcsec seeing. In contrast, the MaNGA and CALIFA cubes have an effective FWHM of ~ 2.5 arcsec, meaning that for a centrally concentrated source there will be systematically less flux within a 3 arcsec diameter aperture within these cubes than in the original SDSS-I single-fiber spectrum. We therefore extract the corresponding MaNGA and CALIFA spectra in a five-arcsecond-diameter circular aperture about the nominal location of the SDSS-I spectrum, and additionally allow for a constant multiplicative scaling factor between all of the spectra (derived from the average ratio of the spectra interpolated to a common wavelength solution).

In Figure 20 we plot the resulting spectra for the SDSS-I (red line), SDSS-IV/MaNGA (black line), and CALIFA $R \sim 850$ (green line) and $R \sim 1650$ (blue line) data. Although we cannot assess the absolute flux calibration from this plot, we note that

⁵⁴ The rms of any individual line is closely related to the strength of the line (stronger lines have smaller rms), and the wavelength solution is based upon a fit to many such lines (both skylines and arc-lamp lines).

⁵⁵ Based on observations collected at the Centro Astronómico Hispano Alemán (CAHA) at Calar Alto, operated jointly by the Max-Planck-Institut für Astronomie and the Instituto de Astrofísica de Andalucía (CSIC). See <http://califa.caha.es/>.

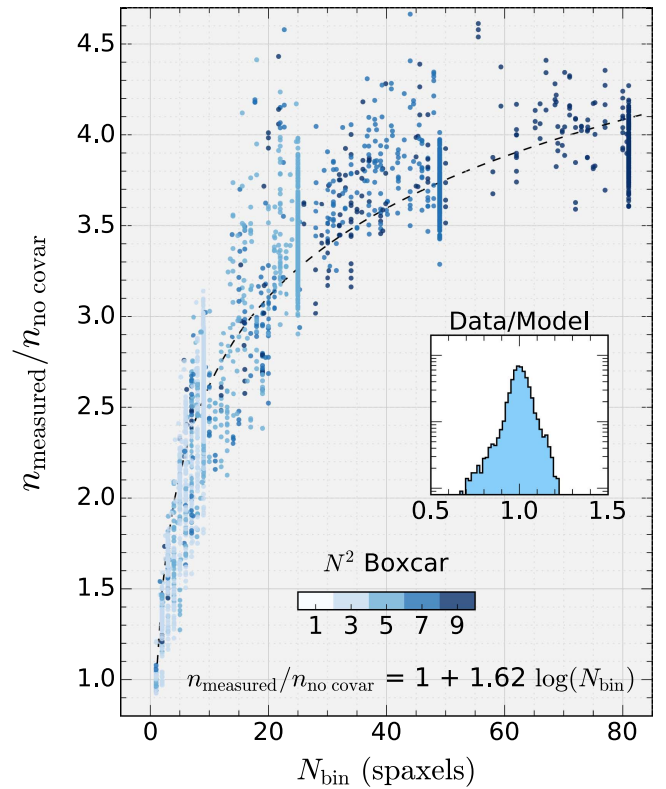


Figure 16. Ratio of the measured noise in a synthetic data cube, n_{measured} , (see text) to a nominal calculation of the noise in a binned spectrum that does not include covariance, $n_{\text{no covar}}$, as a function of the number of spaxels included in the combined spectrum, N_{bin} . The point color provides the size of the boxcar used to create the bin. Nominally, $N_{\text{bin}} = N^2$, however some boxcar windows fell outside of the IFU field-of-view in the synthetic data cube. The equation at the bottom right gives the best-fitting calibration of $n_{\text{no covar}}$ to n_{measured} for values of $N_{\text{bin}} \leq 100$. The inset histogram shows the ratio of the model to the data, demonstrating that the calibration is good to about 30%.

the *relative* flux calibration between the four spectra is in extremely good agreement. In the regions of common wavelength coverage, all four spectra show similar structure in the continuum and the emission/absorption lines, with the exception of a known downturn due to vignetting in the CALIFA low-resolution spectrum longward of 7100 \AA . Figure 20 also clearly demonstrates the longer wavelength baseline and higher S/N (especially in the far blue) of the MaNGA data compared to both SDSS-I and CALIFA.

Additionally, we estimate the typical sensitivity of the MaNGA data cubes based on the inverse variance reported by the pipeline for regions far along the minor axis away from edge-on disk galaxy 8465–12704. We estimate the typical continuum surface brightness sensitivity by taking the square root of the sum of the variances of cube spaxels within a five-arcsecond-diameter region, multiplying by a covariance correction factor based on the number of spatial elements summed (see Equation (9)), and converting the resulting 1σ flux sensitivity to a 10σ sensitivity in terms of AB surface brightness. Similarly, to determine the typical 5σ point source emission line sensitivity we sum the variance over twice the FWHM of the LSF, sum over a five-arcsecond-diameter aperture, and multiply the square root of this by a covariance correction factor. We note that both sensitivity estimates include only noise from the detector and background sky, and do not account for any additional noise that may be introduced

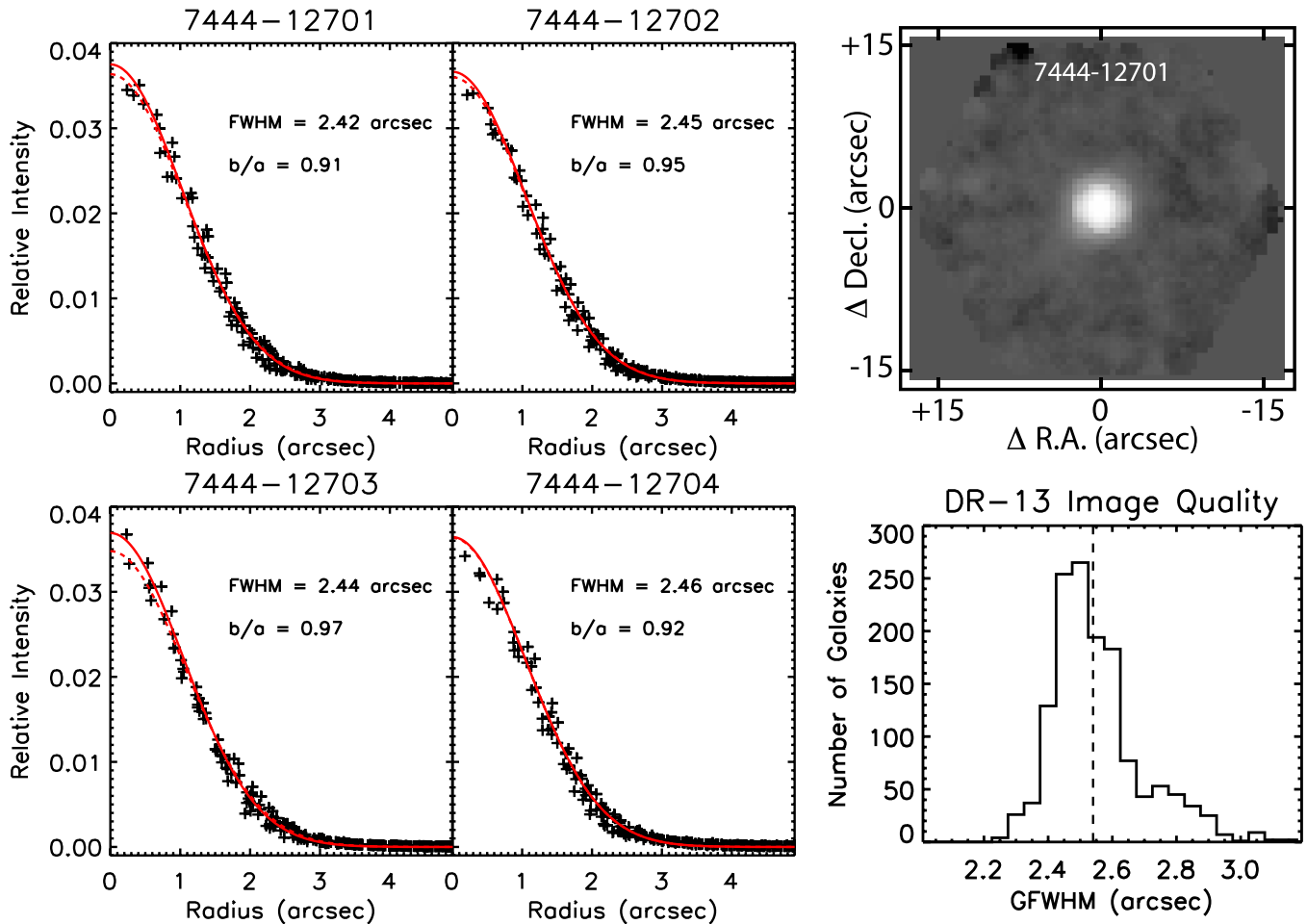


Figure 17. Top right panel: reconstructed image of a bright star observed in standard dithered observations (7444-12701); the data cube has been collapsed over wavelength channels 300–700 ($\lambda\lambda 3881\text{--}4255$ Å). The grayscale stretch is logarithmic to illustrate the symmetrical nature of the extended profile wings. Left-hand panels: radial profiles of bright stars targeted by four of the largest IFUs on plate 7444. Black points show the radial profile of the reconstructed image (based on collapsing the corresponding data cube over the range $\lambda\lambda 3881\text{--}4255$ Å). The solid red lines show the best 2D Gaussian fitted to the black points, with characteristic FWHM and minor/major axis ratio (b/a) indicated. The dashed red lines show the corresponding 2D Gaussian fitted to the PSF model provided by the pipeline based on known fiber locations and observing conditions for each exposure. Lower right panel: Distribution of g -band FWHM measured for all 1390 galaxy data cubes in DR13; the vertical dashed line indicates the median of 2.54 arcsec.

by astrophysical sources. As illustrated in Figure 21, the derived sensitivities within a five-arcsecond-diameter aperture are strong functions of wavelength, varying from about $23.5 \text{ AB arcsec}^{-2}$ and $5 \times 10^{-17} \text{ erg s}^{-1} \text{ cm}^{-2}$ at blue wavelengths to about $20 \text{ AB arcsec}^{-2}$ and $2 \times 10^{-16} \text{ erg s}^{-1} \text{ cm}^{-2}$ in the vicinity of the strongest OH skylines.

11. SUMMARY

The 13th data release of the Sloan Digital Sky Survey includes the raw MaNGA spectroscopic data, the fully reduced spectrophotometrically calibrated data, and the pipeline software and metadata required for individual users to re-reduce the data themselves. In this work, we have described the framework and algorithms of the MaNGA DRP software MANGADRP version v1_5_4 and the format and quality of the ensuing reduced data products. The DRP operates in two stages; the first stage performs optimal extraction, sky subtraction, and flux calibration of individual frames, while the second combines multiple frames together with astrometric information to create calibrated individual fiber spectra (in a row-stacked format) and rectified coadded

data cubes for each target galaxy. The RSS and coadded data cubes are provided for both a linear and a logarithmically sampled wavelength grid, both covering the wavelength range 3622–10354 Å.

For the 1390 galaxy data cubes released in DR13 we demonstrate that the MaNGA data have nearly Poisson-limited sky subtraction shortward of ~ 8500 Å, with a residual pixel value distribution in all-sky test plates nearly consistent with a Gaussian distribution whose width is determined by the expected contributions from detector and Poisson noise.

Each MaNGA exposure is flux calibrated independently of all other exposures using mini-bundles placed on spectrophotometric standard stars; based on comparison to broadband imaging the composite data cubes have a typical relative calibration of 1.7% (between $H\beta$ and $H\alpha$) with an absolute calibration of better than 5% for more than 89% of the MaNGA wavelength range. These data cubes reach a typical 10σ limiting continuum surface brightness $\mu = 23.5 \text{ AB arcsec}^{-2}$ in a five-arcsecond-diameter aperture in the g -band. Additionally, we have demonstrated the following.

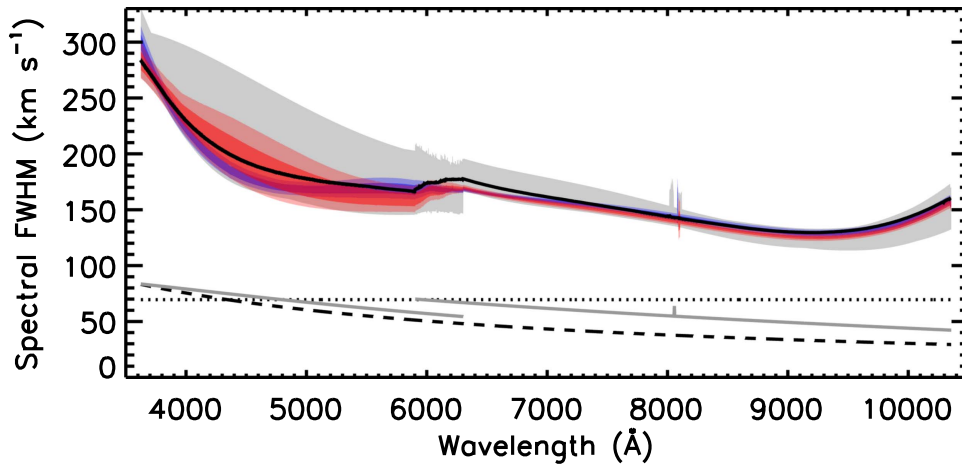


Figure 18. MaNGA spectral resolution (FWHM) as a function of wavelength for the final wavelength-rectified data products. The solid black line represents the average FWHM across all 1390 galaxy data cubes in DR13, while the gray shaded region indicates the minimum and maximum FWHM of all 11,916 fiber spectra obtained for example plate 8588. Blue dark/light shaded regions and red dark/light shaded regions show the $1\sigma/2\sigma$ variations about the the least-variable and most-variable IFUs on this plate, respectively (8588–12704 and 8588–12705). The dotted and dashed black lines indicate the final pixel sampling scale of the MaNGA LOG-format and LINEAR-format data, respectively. The solid gray lines represent the native pixel sampling of the blue and red cameras. The feature around 8100 Å indicates the two-phase detector discontinuity. Note that the values shown here have been broadened by 10% relative to the values reported by the DR13 data pipeline to account for post-pixellization modeling and wavelength rectification (see discussion in Section 10.2).

1. The wavelength calibration of the MaNGA data has an absolute accuracy of 5 km s^{-1} rms with a relative fiber-to-fiber accuracy of better than 1 km s^{-1} rms.
2. The astrometric accuracy of the reconstructed MaNGA data cubes is typically 0.1 arcsec rms, based on comparison to previous SDSS broadband imaging.
3. The spatial resolution of the MaNGA data is a function of the observational seeing, with a median of 2.54 arcsec FWHM. We have shown that the effective reconstructed point source profile is well described by a single Gaussian whose parameters are given in the header of each data cube.
4. The spectral resolution of the MaNGA data is a function of both both fiber number and wavelength, but has a median $\sigma = 72 \text{ km s}^{-1}$.

Despite these overall successes of the MaNGA DRP, we conclude by noting that there is still ample room for future improvements to be made in some key areas. First, sky subtraction (while adequate for most purposes) shows some non-gaussianities in the residual distribution, a slight overestimate in the read noise of one camera, and a possible systematic oversubtraction at the $\sim 0.1\sigma$ level in the blue. Work is ongoing to test whether better treatment of amplifier crosstalk or the scattered light model can improve limiting performance in this area for the purposes of extremely deep spectral stacking. Second, the spectral LSFs given in the DR13 data products (and in previous SDSS optical fiber spectra) are effectively underreported by about 10%. Work is currently underway to use high spectral resolution observations of MaNGA target galaxies to constrain this effect more precisely and fix it in future data releases. Third, spatial covariance in the reconstructed data cubes (treated here by a simple functional approximation) can also be treated more completely. Finally, with additional data it will be possible to fine tune the MaNGA quality-control algorithms (which currently can be overly aggressive in flagging potentially

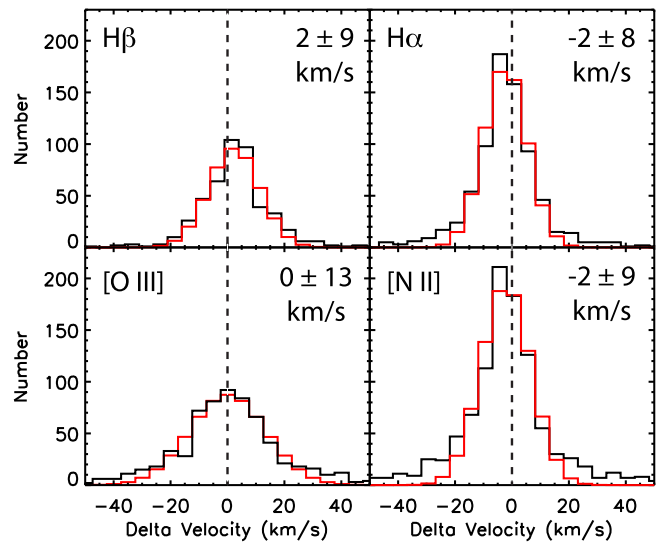


Figure 19. Histograms of velocity difference between SDSS-I spectra and MaNGA IFU spectra extracted from a 2 arcsec radius circular aperture centered on the location of the SDSS-I spectra. The four panels show the results for $\text{H}\beta$, $[\text{O III}] \lambda 5007$, $\text{H}\alpha$, and $[\text{N II}] \lambda 6583$ for the 1351 unique galaxies in DR13. Note that the many galaxies with nebular emission lines too weak for reliable measurement have been omitted from the distribution. Black histograms in each panel show the observed distribution, while red histograms illustrate the best-fit Gaussian model. The values in each panel give the center and 1σ width of the Gaussian model; this width may be driven largely by internal velocity gradients paired with uncertainties in the SDSS-I fiber locations.

problematic cases) and likely recover some of the objects whose reduced data have been identified as unreliable for use in DR13.

This work was supported by the World Premier International Research Center Initiative (WPI Initiative), MEXT,

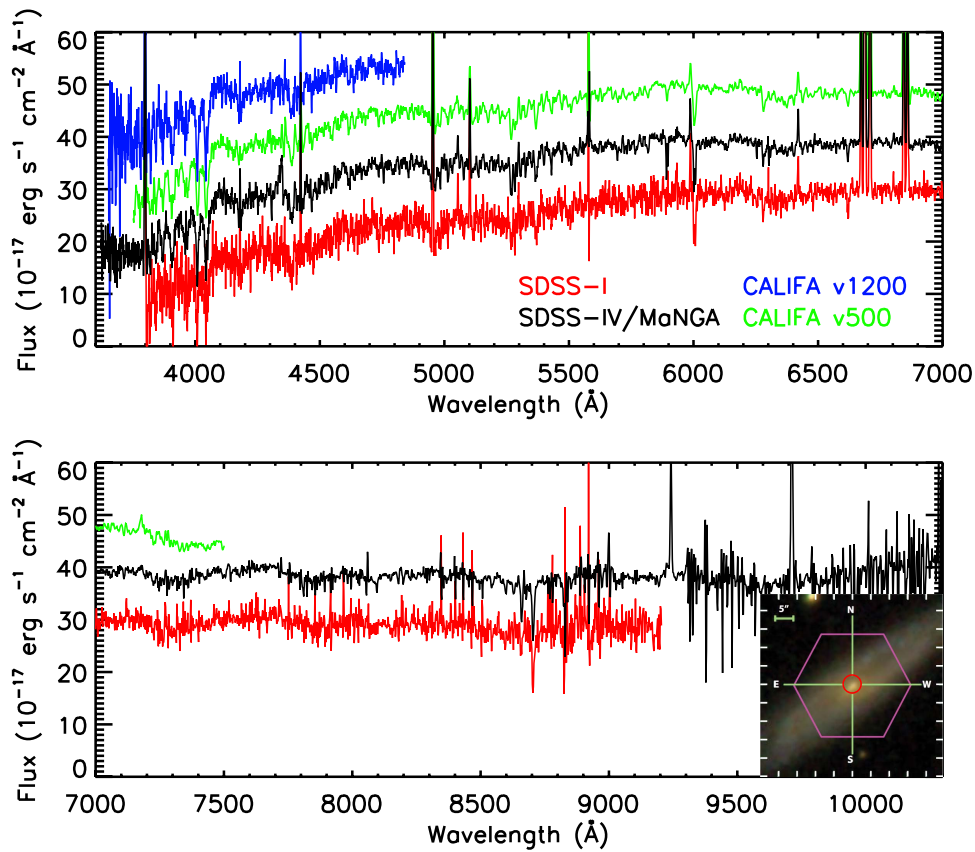


Figure 20. Central spectrum of galaxy 7443–12704 (UGC 09873) extracted from the SDSS-IV MaNGA IFU data cube (black line) compared to the co-located SDSS-I single-fiber spectrum (red line). For comparison we also include spectra extracted from the CALIFA high-resolution (v1200; blue line) and low-resolution (v500; green line) IFU data cubes. SDSS-I and CALIFA spectra have been offset vertically from the MaNGA spectrum to aid visual inspection. The inset at lower right shows the SDSS three-color image of UGC 09873 along with an indication of the MaNGA IFU footprint (pink hexagon) and circular spectral extraction region (red circle).

Japan. A.W. acknowledges support of a Leverhulme Trust Early Career Fellowship. M.A.B. acknowledges support from NSF AST-1517006. G.B. is supported by CONICYT/FONDECYT, Programa de Iniciacion, Folio 11150220. Funding for the Sloan Digital Sky Survey IV has been provided by the Alfred P. Sloan Foundation and the Participating Institutions. SDSS-IV acknowledges support and resources from the Center for High-Performance Computing at the University of Utah. The SDSS web site is www.sdss.org.

SDSS-IV is managed by the Astrophysical Research Consortium for the Participating Institutions of the SDSS Collaboration including the Carnegie Institution for Science, Carnegie Mellon University, the Chilean Participation Group, Harvard-Smithsonian Center for Astrophysics, Instituto de Astrofísica de Canarias, The Johns Hopkins University, Kavli Institute for the Physics and Mathematics of the universe (IPMU)/University of Tokyo, Lawrence Berkeley National Laboratory, Leibniz Institut für Astrophysik Potsdam (AIP), Max-Planck-Institut für Astrophysik (MPA Garching), Max-Planck-Institut für Extraterrestrische Physik (MPE), Max-Planck-Institut für Astronomie (MPIA Heidelberg), National Astronomical Observatory of China, New Mexico State University, New York University, The Ohio State University, Pennsylvania State University, Shanghai Astronomical Observatory, United Kingdom Participation Group, Universidad Nacional Autónoma de México, University of Arizona, University of Colorado Boulder,

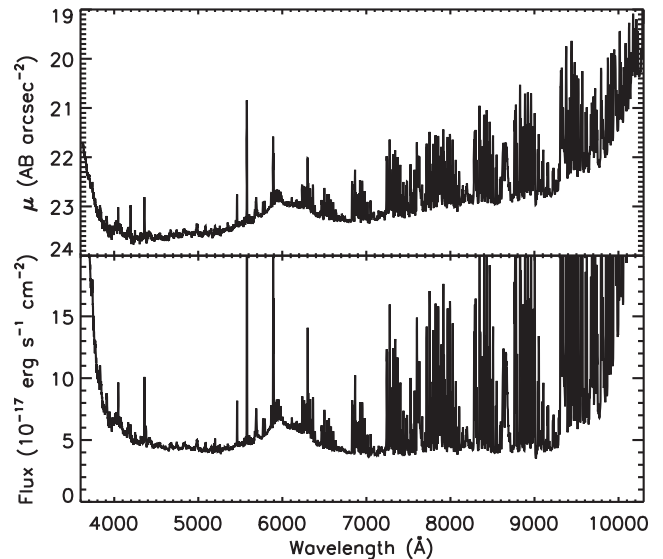


Figure 21. Top panel: MaNGA 10σ limiting continuum surface brightness sensitivity within a five-arcsecond-diameter aperture. Bottom panel: MaNGA 5σ limiting line sensitivity for a spectrally unresolved emission line in a five-arcsecond-diameter aperture. Both panels are based on the off-axis region far from the edge-on galaxy 8465–12704.

University of Portsmouth, University of Utah, University of Washington, University of Wisconsin, Vanderbilt University, and Yale University.

APPENDIX A
KEY DIFFERENCES BETWEEN
MANGADRP AND IDLSPEC2D

As discussed in previous section, the 2D stage of the MaNGA DRP (i.e., raw data through flux calibrated individual exposures) is derived in large part from the IDLSPEC2D software that has been widely used in one form or another from the original SDSS spectroscopic survey (Abazajian et al. 2003), to the BOSS and eBOSS surveys (Dawson et al. 2013, 2016), to the DEEP2 survey (Newman et al. 2013). Given this legacy, we summarize here for ease of reference the key differences between our implementation of this code and its implementation during the BOSS survey for DR12.

1. Spectral Pre-processing (Section 4.1): MANGADRP and IDLSPEC2D use nearly identical algorithms, except that for MaNGA the cosmic-ray identification routine is run twice to flag additional features missed the first time.
2. Spatial Fiber Tracing (Section 4.2.1): The MANGADRP fiber tracing code is substantially different from that used by IDLSPEC2D. For BOSS, the initial fiber locations in the starting row were determined by locating peaks and determining which block of fibers a given peak must belong to (and which fibers were missing) based on the known (and constant) number of fibers in each v-groove block. This method proved unreliable for MaNGA given the variable number of fibers per block and different potential failure modes (in particular, if a large IFU falls out of the plate during observations there can be large regions of the detector with only the block-edge sky fibers plugged). After implementing a cross-correlation technique based on the known nominal locations of each fiber, the MaNGA tracing routine has proven robust against all hardware failure modes.

The fine adjustment of the flux-weighted fiber centroids in each row using cross-correlation of a Gaussian model is also new to the MANGADRP code.

3. Scattered Light (Section 4.2.3): The bspline scattered light routine implemented in MANGADRP for bright-time data and flat-fields is entirely new compared to IDLSPEC2D.
4. Spectral Extraction (Section 4.2.2): The spectral extraction technique used by MANGADRP is similar to that of IDLSPEC2D. However, MaNGA uses the C-based implementation of the extraction used by the original SDSS-I survey (which extracts an entire detector row at a time) while BOSS and eBOSS use an IDL-based implementation that operates on a given v-groove block of fibers at a time. We found the latter to be undesirable for MaNGA since discrete processing of individual blocks can produce discontinuities in the background term that can be seen in the reduced all-sky data when a given IFU covers more than one block.

Additionally, MaNGA fits the derived fiber widths in a given v-groove block by a linear relation as a function of fiberid where BOSS uses a constant value for each block.

5. Fiber Flat-field (Section 4.2.4): The fiber flat-field technique is nearly identical between MANGADRP and IDLSPEC2D.
6. Wavelength and LSF calibration (Section 4.2.5): The initial wavelength solution and LSF estimate based on the

arc-lamp calibration frames is nearly identical between MANGADRP and IDLSPEC2D, with the exception that MaNGA fits the derived LSF in a given v-groove block by a linear relation as a function of fiberid where BOSS uses a constant value for each block.

7. Science Frame extraction (Section 4.3): The science frame extraction process is largely similar between MANGADRP and IDLSPEC2D, with the exception that BOSS makes no correction to the derived arc-line LSF based on the skylines.
8. Sky subtraction (Section 5): Although the general approach to sky subtraction is similar between MANGADRP and IDLSPEC2D, in the sense that both use basis splines to build a super-sampled sky model, the practical implementation differs substantially. This difference is largely due to the fundamental hardware differences between the two surveys; where BOSS has 1000 fibers (science plus sky and standard) distributed nearly randomly across the entire 3° field, MaNGA effectively has large groups of fibers clustered at the same few locations on-sky with outrigger sky fibers surrounding them. This means that MaNGA samples a more discrete and discontinuous assortment of background sky locations, but can similarly use the locality of sky and IFU fibers to constrain the background local to a given IFU. In contrast to the assortment of scaling factors, smoothed inverse variance weighting, local sky adjustments, and 1D and 2D sky models used by MaNGA, BOSS simply uses a 2D basis-spline model of the sky background evaluated at the wavelengths of each fiber (although we note that eBOSS has also recently adopted a smoothed inverse variance weighting scheme similar to ours in order to avoid systematic undersubtraction of the sky background present in the previous BOSS reductions).
9. Flux calibration (Section 6): As discussed by Yan et al. (2016a), flux calibration techniques differ substantially between MANGADRP and IDLSPEC2D since MaNGA and BOSS are attempting to solve different problems. While BOSS must correct for both system throughput losses and geometric fiber aperture losses, MaNGA must disentangle the two and correct only for system losses. Although the core of the stellar spectral library comparison is thus shared between the two codes, the implementation differs dramatically.
10. Wavelength rectification (Section 7): The spline-based approach to the wavelength rectification is common between both MANGADRP and IDLSPEC2D, but MaNGA uses a smoothed inverse-variance weighting approach where BOSS used simple inverse variance weighting (this has since been updated to smoothed inverse variance for eBOSS). MaNGA also uses a slightly different breakpoint spacing, and evaluates the bspline fit on both a logarithmic and a linear wavelength solution. The second-pass cosmic-ray identification by growing the previous cosmic-ray mask is also unique to MaNGA.
11. Quality control (Section 3.4): The DRP2QUAL infrastructure to evaluate frame quality and stop reduction at various points if necessary is entirely new to MANGADRP.

APPENDIX B MaNGA DATA MODEL

We provide here for convenient reference an overview of the primary data products delivered by the MaNGA DRP. These are in the format of gzipped multi-extension FITS files, with a mixture of image data and binary table extensions. For a detailed description including definitions of keyword headers see the online DR13 documentation at <http://www.sdss.org/dr13/manga/manga-data/data-model/>. This appendix is split into four sections: Appendix B.1 describes the intermediate (2D DRP) products, Appendix B.2 describes the final (3D DRP) products, Appendix B.3 describes the “drpall” summary table product, and Appendix B.4 describes the key 3D pipeline quality bitmasks.

B.1. Intermediate DRP Data Products

The intermediate data products are produced by the 2D stage of the MaNGA DRP. These products are output during the calibration, flux extraction, sky subtraction, and flux calibration stages of the pipeline. In Figure 22 we show examples of the primary data extension of these types of files. In Tables 4–9 we give the structure of the intermediate and calibration FITS files. For the intermediate data products, the naming convention includes the camera name (except for the camera-combined mgCFrame file), and the zero-padded exposure number. Since the MaNGA instrument has two spectrographs each with a red and blue camera, there are four camera designations: b1, r1, b2, and r2.

B.1.1. mgArc

These are the extracted arc frames, produced during wavelength calibration. The format is similar to the BOSS spArc file, with the exception of a blank extension 0 and extension names instead of numbers.

Written by: https://svn.sdss.org/public/repo/manga/mangadrp/tags/v1_5_4/pro/spec2d/mdrp_calib.pro
Data Model: https://data.sdss.org/datamodel/files/MANGA_SPECTRO_REDUX/DRPVER/PLATE4/MJD5/mgArc.html

B.1.2. mgFlat

These are the extracted flat-field frames, produced after the fiber tracing, wavelength calibration, and global quartz lamp spectrum have been removed. The format is similar to the BOSS spFlat files, with the exception of a blank extension 0 and extension names instead of numbers.

Written by: https://svn.sdss.org/public/repo/manga/mangadrp/tags/v1_5_4/pro/spec2d/mdrp_calib.pro
Data Model: https://data.sdss.org/datamodel/files/MANGA_SPECTRO_REDUX/DRPVER/PLATE4/MJD5/mgFlat.html

B.1.3. mgFrame

These are the extracted fiber spectra for each camera for the science exposures.

Written by: https://svn.sdss.org/public/repo/manga/mangadrp/tags/v1_5_4/pro/spec2d/mdrp_extract_object.pro

Data Model: https://data.sdss.org/datamodel/files/MANGA_SPECTRO_REDUX/DRPVER/PLATE4/MJD5/mgFrame.html

B.1.4. mgSFrame

These are the science fiber spectra for each camera after the sky subtraction routine has been applied to the mgFrame files (the “S” in mgSFrame stands for Sky Subtracted).

Written by: https://svn.sdss.org/public/repo/manga/mangadrp/tags/v1_5_4/pro/spec2d/mdrp_skysubtract.pro

Data Model: https://data.sdss.org/datamodel/files/MANGA_SPECTRO_REDUX/DRPVER/PLATE4/MJD5/mgSFrame.html

B.1.5. mgFFrame

These are the science fiber spectra for each camera after the flux calibration routine has been applied to the mgSFrame files (the “F” in mgFFrame stands for Flux calibrated).

Written by: https://svn.sdss.org/public/repo/manga/mangadrp/tags/v1_5_4/pro/spec2d/mdrp_fluxcal.pro
Data Model: https://data.sdss.org/datamodel/files/MANGA_SPECTRO_REDUX/DRPVER/PLATE4/MJD5/mgFFrame.html

B.1.6. mgCFrame

These are the science fiber spectra after the individual-camera flux-calibrated mgFFrame files have been combined together across the dichroic break and fibers from spectrograph 2 have been appended atop those from spectrograph 1 (i.e., in order of increasing fiberid). All spectra in this file have been resampled to a common wavelength grid across the entire MaNGA survey using a basis-spline technique described in Section 7 (the “C” in mgCFrame stands for Calibrated and Camera Combined on a Common wavelength grid). There are two versions of this file; the first uses a logarithmic wavelength sampling from $\log_{10}(\lambda/\text{\AA}) = 3.5589$ to 4.0151 (NWAVE = 4563 spectral elements). The second uses a linear wavelength sampling running from 3622.0 to 10353.0 Å (NWAVE = 6732 spectral elements).

Written by: https://svn.sdss.org/public/repo/manga/mangadrp/tags/v1_5_4/pro/spec2d/mdrp_combinecameras.pro

Data Model: https://data.sdss.org/datamodel/files/MANGA_SPECTRO_REDUX/DRPVER/PLATE4/MJD5/mgCFrame.html

B.2. Final DRP Data Products

Depending on the science case, different final summary products are desirable. The MaNGA DRP provides both RSS files and regularly gridded combined data cubes, with both logarithmic and linear wavelength solutions.

These have the naming convention of manga-[PLATEID]-[IFUDESIGN]-[BIN][MODE].fits.gz. PLATEID refers to the

Table 4
mgArc-[camera]-[exposure] Data Structure

HDU	Extension Name	Format	Description
0	Empty except for global header
1	FLUX	[CCDROW \times NFIBER]	Extracted arc-lamp spectra
2	LXPEAK	[NFIBER+1 \times NLAMP]	Wavelengths and x -positions of arc-lamp lines.
3	WSET	[BINARY FITS TABLE]	Wavelength solution as Legendre polynomials for all fibers
4	MASK	[NFIBER]	Fiber bitmask (MANGA_DRP2PIXMASK)
5	DISPSET	[BINARY FITS TABLE]	Spectral LSF (1σ) in pixels as Legendre polynomials for each fiber

Note. NFIBER is the number of fibers in the camera, CCDROW the number of rows on the detector, and NLAMP the number of bright arc lines.

Table 5
mgFlat-[camera]-[exposure] Data Structure

HDU	Extension Name	Format	Description
0	Empty except for global header
1	FLUX	[CCDROW \times NFIBER]	Extracted flat-field lamp spectra
2	TSET	[BINARY FITS TABLE]	Legendre polynomial traceset containing the x , y centers of the fiber traces
3	MASK	[NFIBER]	Fiber bitmask (MANGA_DRP2PIXMASK)
4	WIDTH	[CCDROW \times NFIBER]	Profile cross-dispersion width (1σ) of each fiber
5	SUPERFLATSET	[BINARY FITS TABLE]	Legendre polynomial traceset describing the quartz lamp response function

Table 6
mgFrame-[camera]-[exposure] Data Structure

HDU	Extension Name	Format	Description
0	Empty except for global header
1	FLUX	[CCDROW \times NFIBER]	Extracted spectra in units of flatfielded electrons
2	IVAR	[CCDROW \times NFIBER]	Inverse variance of the extracted spectra
3	MASK	[CCDROW \times NFIBER]	Pixel mask (MANGA_DRP2PIXMASK)
4	WSET	[BINARY FITS TABLE]	Legendre polynomial coefficients describing wavelength solution in $\log_{10} \text{Å}$ (vacuum heliocentric)
5	DISPSET	[BINARY FITS TABLE]	Legendre polynomial coefficients describing spectral LSF (1σ) in pixels
6	SLITMAP	[BINARY FITS TABLE]	Slitmap structure describing plugged plate configuration
7	XPOS	[CCDROW \times NFIBER]	X position of fiber traces on detector
8	SUPERFLAT	[CCDROW \times NFIBER]	Superflat vector from the quartz lamps

Table 7
mgSFrame-[camera]-[exposure] Data Structure

HDU	Extension Name	Format	Description
0	Empty except for global header
1	FLUX	[CCDROW \times NFIBER]	Sky-subtracted spectra in units of flatfielded electrons
2	IVAR	[CCDROW \times NFIBER]	Inverse variance of the sky-subtracted spectra
3	MASK	[CCDROW \times NFIBER]	Pixel mask (MANGA_DRP2PIXMASK)
4	WSET	[BINARY FITS TABLE]	Legendre polynomial coefficients describing wavelength solution in $\log_{10} \text{Å}$ (vacuum heliocentric)
5	DISPSET	[BINARY FITS TABLE]	Legendre polynomial coefficients describing spectral LSF (1σ) in pixels
6	SLITMAP	[BINARY FITS TABLE]	Slitmap structure describing plugged plate configuration
7	XPOS	[CCDROW \times NFIBER]	X position of fiber traces on detector
8	SUPERFLAT	[CCDROW \times NFIBER]	Superflat vector from the quartz lamps
9	SKY	[CCDROW \times NFIBER]	Subtracted model sky spectra in units of flatfielded electrons

four- or five-digit plate identifier. IFUDESIGN refers to the design id of the IFU bundle. BIN refers to the wavelength sampling of the output data product, LOG for logarithmic sampling, or LIN for linear sampling. MODE refers to the

output structure, whether an RSS file or a CUBE file. The combination of plateID-ifuDesign provides a unique identifier to a MaNGA target, and output final-DRP products. While the identifier of manga-id maps to a unique galaxy, it does not map

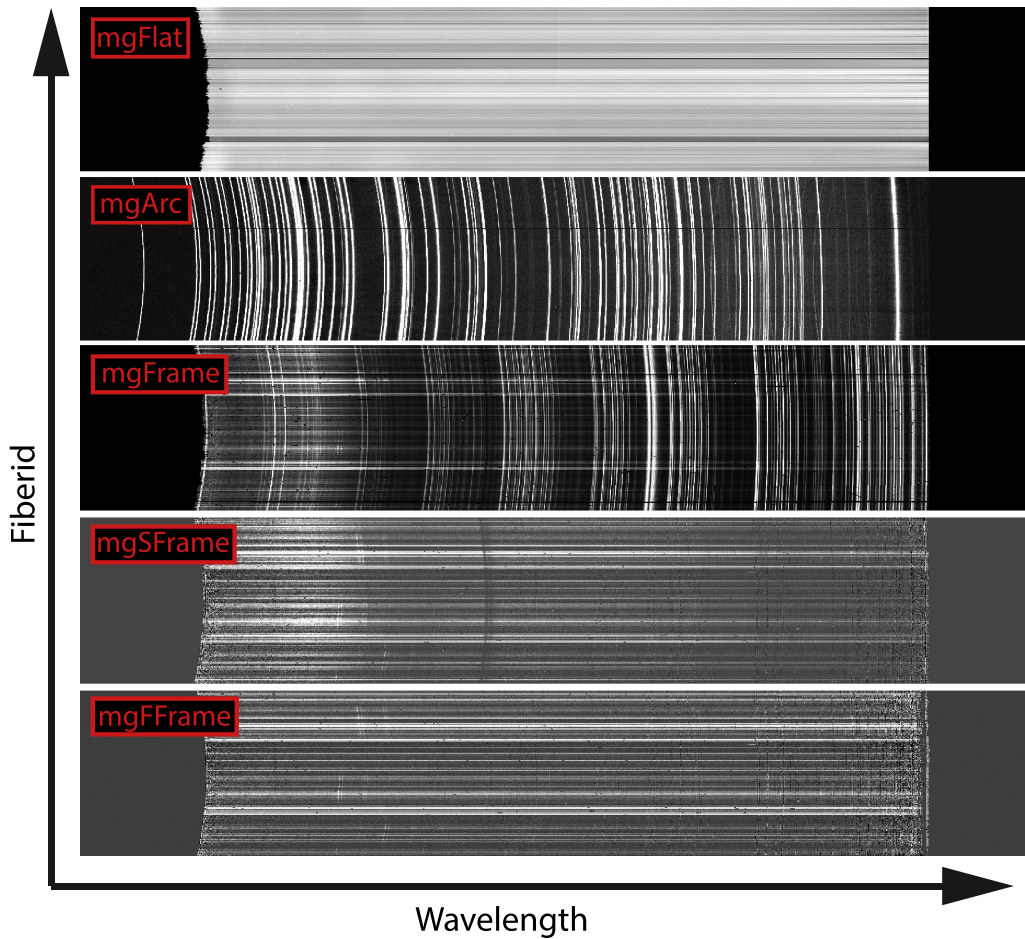


Figure 22. MaNGA intermediate data products from individual exposures. Shown here are extracted fiber flats (mgFlat), arc-lamp spectra (mgArc), extracted science frame spectra (mgFrame), sky-subtracted science frame spectra (mgSFrame), and flux-calibrated science frame spectra (mgFFrame). Note the curvature of the wavelength solution along the spectroscopic slit. The examples shown here are for the r2 camera. The grayscale stretch on the fiberflat image runs from 0.6 to 1.1.

Table 8
mgFFrame-[camera]-[exposure] Data Structure

HDU	Extension Name	Format	Description
0	Empty except for global header
1	FLUX	[CCDROW \times NFIBER]	Flux-calibrated spectra in units of 10^{-17} erg s $^{-1}$ cm $^{-2}$ \AA^{-1} fiber $^{-1}$
2	IVAR	[CCDROW \times NFIBER]	Inverse variance of the flux-calibrated spectra
3	MASK	[CCDROW \times NFIBER]	Pixel mask (MANGA_DRP2PIXMASK)
4	WSET	[BINARY FITS TABLE]	Legendre polynomial coefficients describing wavelength solution in \log_{10} \AA (vacuum heliocentric)
5	DISPSET	[BINARY FITS TABLE]	Legendre polynomial coefficients describing spectral LSF (1σ) in pixels
6	SLITMAP	[BINARY FITS TABLE]	Slitmap structure describing plugged plate configuration
7	XPOS	[CCDROW \times NFIBER]	X position of fiber traces on detector
8	SUPERFLAT	[CCDROW \times NFIBER]	Superflat vector from the quartz lamps
9	SKY	[CCDROW \times NFIBER]	Subtracted model sky spectra in units of 10^{-17} erg s $^{-1}$ cm $^{-2}$ \AA^{-1} fiber $^{-1}$

to a unique set of output data products. If a given galaxy is observed on more than one plate, it will have different final-DRP outputs associated with it by default.

The RSS files (Table 10) are a two-dimensional array in row-stacked-spectra format with horizontal size N_{spec} and vertical size $N = \sum N_{\text{fiber}}(i)$ where $N_{\text{fiber}}(i)$ is the number of fibers in the IFU targeting this galaxy for the i 'th exposure and the sum runs over all exposures. In contrast, the cubes (Table 11) are three-dimensional arrays in which the first and second

dimensions are spatial (with regular 0.5 arcsec square spaxels) and the third dimension represents wavelength.

In each case, there are associated image extensions describing the inverse variance, pixel mask, and a binary table ‘‘OBSINFO’’ that describes full information about each exposure that was combined to produce the final file (exposure number, integration time, hour angle, seeing, etc.). This structure is appended to each file with one line per exposure (Table 12) both for quality-control purposes (so

Table 9
mgCFrame-[exposure] Data Structure

HDU	Extension Name	Format	Description
0	Empty except for global header
1	FLUX	[NWAVE × NFIBER]	Camera-combined, resampled spectra in units of 10^{-17} erg s $^{-1}$ cm $^{-2}$ Å $^{-1}$ fiber $^{-1}$
2	IVAR	[NWAVE × NFIBER]	Inverse variance of the camera-combined spectra
3	MASK	[NWAVE × NFIBER]	Pixel mask (DRP2PIXMASK)
4	WAVE	[NWAVE]	Wavelength vector in units of Å (vacuum heliocentric)
5	DISP	[NWAVE × NFIBER]	Spectral resolution (1σ LSF) in units of Å
6	SLITMAP	[BINARY FITS TABLE]	Slitmap structure describing plugged plate configuration
9	SKY	[NWAVE × NFIBER]	Resampled model sky spectra in units of 10^{-17} erg s $^{-1}$ cm $^{-2}$ Å $^{-1}$ fiber $^{-1}$

Note. Both LINEAR and LOG-format versions of this file are produced, with either logarithmic or linear wavelength sampling respectively. NWAVE is the total number of wavelength channels (6732 for LINEAR, 4563 for LOG). NFIBER = 1423 total fibers.

Table 10
manga-[plate]-[ifudesign]-LOGRSS Data Structure

HDU	Extension Name	Format	Description
0	Empty except for global header
1	FLUX	[NWAVE × (NFIBER × NEXP)]	Row-stacked spectra in units of 10^{-17} erg s $^{-1}$ cm $^{-2}$ Å $^{-1}$ fiber $^{-1}$
2	IVAR	[NWAVE × (NFIBER × NEXP)]	Inverse variance of row-stacked spectra
3	MASK	[NWAVE × (NFIBER × NEXP)]	Pixel mask (MANGA_DRP2PIXMASK)
4	DISP	[NWAVE × (NFIBER × NEXP)]	Spectral LSF (1σ) in units of Å
5	WAVE	[NWAVE]	Wavelength vector in units of Å (vacuum heliocentric)
6	SPECRES	[NWAVE]	Median spectral resolution versus wavelength
7	SPECRESD	[NWAVE]	Standard deviation (1σ) of spectral resolution versus wavelength
8	OBSINFO	[BINARY FITS TABLE]	Table detailing exposures combined to create this file.
9	XPOS	[NWAVE × (NFIBER × NEXP)]	Array of fiber X -positions (units of arcseconds) relative to the IFU center
10	YPOS	[NWAVE × (NFIBER × NEXP)]	Array of fiber Y -positions (units of arcseconds) relative to the IFU center

Note. Both LINEAR and LOG-format versions of this file are produced, with either logarithmic or linear wavelength sampling respectively. NWAVE is the total number of wavelength channels (6732 for LINEAR, 4563 for LOG). NFIBER is the number of fibers in the IFU; NEXP is the number of exposures.

Table 11
manga-[plate]-[ifudesign]-LOGCUBE Data Structure

HDU	Extension Name	Format	Description
0	Empty except for global header
1	FLUX	[NX × NY × NWAVE]	3D rectified cube in units of 10^{-17} erg s $^{-1}$ cm $^{-2}$ Å $^{-1}$ spaxel $^{-1}$
2	IVAR	[NX × NY × NWAVE]	Inverse variance cube
3	MASK	[NX × NY × NWAVE]	Pixel mask cube (MANGA_DRP3PIXMASK)
4	WAVE	[NWAVE]	Wavelength vector in units of Å (vacuum heliocentric)
5	SPECRES	[NWAVE]	Median spectral resolution versus wavelength
6	SPECRESD	[NWAVE]	Standard deviation (1σ) of spectral resolution versus wavelength
7	OBSINFO	[BINARY FITS TABLE]	Table detailing exposures combined to create this file.
8	GIMG	[NX × NY]	Broadband SDSS g image created from the data cube
9	RIMG	[NX × NY]	Broadband SDSS r image created from the data cube
10	IIMG	[NX × NY]	Broadband SDSS i image created from the data cube
11	ZIMG	[NX × NY]	Broadband SDSS z image created from the data cube
12	GPSF	[NX × NY]	Reconstructed SDSS g point source response profile
13	RPSF	[NX × NY]	Reconstructed SDSS r point source response profile
14	IPSF	[NX × NY]	Reconstructed SDSS i point source response profile
15	ZPSF	[NX × NY]	Reconstructed SDSS z point source response profile

Note. Both LINEAR and LOG-format versions of this file are produced, with either logarithmic or linear wavelength sampling respectively. NWAVE is the total number of wavelength channels (6732 for LINEAR, 4563 for LOG).

that delivered data can be tracked back to individual exposures easily), and so that future forward modeling efforts can read from this extension everything necessary to know about the instrument and observing configuration of each exposure.

Additionally, each RSS-format file has an extension listing the effective X and Y position (calculated by the astrometry module) corresponding to each element in the flux array. Because of chromatic DAR, each wavelength for a given fiber has a slightly different position, and therefore the positional

Table 12
ObsInfo Binary Table Extension

ColumnNo	ColumnName	Format	Description
1	SLITFILE	str	Name of the slitmap
2	METFILE	str	Name of the metrology file
3	HARNAME	str	Harness name
4	IFUDESIGN	int32	ifudesign (e.g., 12701)
5	FRLPLUG	int16	The physical ferrule matching this part of the slit
6	MANGAID	str	MaNGA identification number
7	AIRTEMP	float32	Temperature in Celsius
8	HUMIDITY	float32	Relative humidity in percent
9	PRESSURE	float32	Pressure in inHg
10	SEEING	float32	Best guider seeing in Arcsec
11	PSFFAC	float32	Best-fit PSF size relative to guider measurement
12	TRANSPAR	float32	Guider transparency
13	PLATEID	int32	Plate id number
14	DESIGNID	int32	Design id number
15	CARTID	int16	Cart id number
16	MJD	int32	MJD of observation
17	EXPTIME	float32	Exposure time (seconds)
18	EXPNUM	str	Exposure number
19	SET	int32	Which set this exposure belongs to
20	MGDPOS	str	MaNGA dither position (NSEC)
21	MGDRA	float32	MaNGA dither offset in R.A. (arcsec)
22	MGDDC	float32	MaNGA dither offset in decl. (arcsec)
23–27	OMEGASET_[UGRIZ]	float32	Omega value of this set in <i>ugriz</i> bands at [3622, 4703, 6177, 7496, 10354] Å, respectively
28–39	EAMFIT_[PARAM]	float32	Parameters from the Extended Astrometry Module ^a
40	TAIBEG	str	TAI at the start of the exposure
41	HADRILL	float32	Hour angle plate was drilled for
42	LSTMID	float32	Local sidereal time at midpoint of exposure
43	HAMID	float32	Hour angle at midpoint of exposure for this IFU
44	AIRMASS	float32	Airmass at midpoint of exposure for this IFU
45	IFURA	float64	IFU right ascension (J2000)
46	IFUDEC	float64	IFU declination (J2000)
47	CENRA	float64	Plate center right ascension (J2000)
48	CENDEC	float64	Plate center declination (J2000)
49	XFOCAL	float32	Hole location in xfocal coordinates (mm)
50	YFOCAL	float32	Hole location in yfocal coordinates (mm)
51	MNGTARG1	int32	manga_target1 maskbit for galaxy target catalog
52	MNGTARG2	int32	manga_target2 maskbit for non-galaxy target catalog
53	MNGTARG3	int32	manga_target3 maskbit for ancillary target catalog
54	BLUESN2	float32	SN2 in blue for this exposure
55	REDSN2	float32	SN2 in red for this exposure
56	BLUEPSTAT	float32	Poisson statistic in blue for this exposure
57	REDPSTAT	float32	Poisson statistic in red for this exposure
58	DRP2QUAL	int32	DRP 2D quality bitmask
59	THISBADIFU	int32	0 if good, 1 if this IFU was bad in this frame
60–63	PF_FWHM_[GRIZ]	float32	FWHM (arcsec) of a single-Gaussian fitted to the point source response function Prior to Fiber convolution in bands [<i>griz</i>]

Note.

^a EAM Parameters: R.A., decl., Theta, Theta0, A, B, RAerr, DECerr, ThetaErr, Theta0Err, Aerr, Berr. See https://data.sdss.org/datamodel/files/MANGA_SPECTRO_REDUX/DRPVER/PLATE4/stack/manga-CUBE.html#hdu7 for a full description of the obsinfo data model.

arrays have the same dimensionality as the corresponding flux array. Each data cube also has four extensions corresponding to reconstructed broadband images obtained by convolving the data cube with the SDSS *griz* filter response functions, and four extensions illustrating the reconstructed PSF in the *griz* bands (see discussion in Section 10.1).

As detailed by <http://www.sdss.org/dr13/manga/manga-data/data-model/> there are an assortment of FITS header keycards specifying information such as World Coordinate

Systems (WCS), average reconstructed PSF FWHM in *griz* bandpasses, total exposure time, Milky Way dust extinction, etc. The WCS adopted for the logarithmic wavelength solution follows the CTYPE = WAVE-LOG convention (Greisen et al. 2006) convention in which

$$\lambda = \text{CRVAL}_i \times \exp(\text{CDi}_i \times (p - \text{CRPIX}_i) / \text{CRVAL}_i) \quad (12)$$

Table 13
MANGA_DRP2PIXMASK Data Quality Bits

Bit	Value	Label	Description
Mask bits per fiber			
0	1	NOPLUG	Fiber not listed in plugmap file
1	2	BADTRACE	Bad trace
2	4	BADFLAT	Low counts in fiberflat
3	8	BADARC	Bad arc solution
4	16	MANYBADCOLUMNS	More than 10% of pixels are bad columns
5	32	MANYREJECTED	More than 10% of pixels are rejected in extraction
6	64	LARGESHIFT	Large spatial shift between flat and object position
7	128	BADSKYFIBER	Sky fiber shows extreme residuals
8	256	NEARWHOPPER	Within 2 fibers of a whopping fiber (exclusive)
9	512	WHOPPER	Whopping fiber, with a very bright source.
10	1024	SMEARIMAGE	Smear available for red and blue cameras
11	2048	SMEARHIGHSN	S/N sufficient for full smear fit
12	4096	SMEARMEDSN	S/N only sufficient for scaled median fit
13	8192	DEADFIBER	Broken fiber according to metrology files
Mask bits per pixel			
15	32,768	BADPIX	Pixel flagged in badpix reference file.
16	65,536	COSMIC	Pixel flagged as cosmic-ray.
17	131,072	NEARBADPIXEL	Bad pixel within 3 pixels of trace.
18	262,144	LOWFLAT	Flat-field less than 0.5
19	524,288	FULLREJECT	Pixel fully rejected in extraction model fit (INVVAR = 0)
20	1,048,576	PARTIALREJECT	Some pixels rejected in extraction model fit
21	2,097,152	SCATTEREDLIGHT	Scattered light significant
22	4,194,304	CROSTALK	Cross-talk significant
23	8,388,608	NOSKY	Sky level unknown at this wavelength (INVVAR = 0)
24	16,777,216	BRIGHTSKY	Sky level > flux + 10 * (flux_err) AND sky > 1.25 * median(sky,99 pixels)
25	33,554,432	NODATA	No data available in combine B-spline (INVVAR = 0)
26	671,108,864	COMBINEREJ	Rejected in combine B-spline
27	134,217,728	BADFLUXFACTOR	Low flux calibration or flux-correction factor
28	268,435,456	BADSKYCHI	Relative chi2 > 3 in sky residuals at this wavelength
29	536,870,912	REDMONSTER	Contiguous region of bad chi2 in sky residuals (with threshold of relative chi2 > 3).
30	1,073,741,824	3DREJECT	Used in RSS file, indicates should be rejected when making 3D cube

Table 14
MANGA_DRP3PIXMASK Data Quality Bits

Bit	Value	Label	Description
0	1	NOCOV	No coverage in cube
1	2	LOWCOV	Low coverage depth in cube
2	4	DEADFIBER	Major contributing fiber is dead
3	8	FORESTAR	Foreground star
10	1024	DONOTUSE	Do not use this spaxel for science

B.4. DRP Data Quality Bitmasks

The MaNGA DRP 2D pixel bitmasks applicable to individual reduced frames and composite RSS files are given in Table 13. These indicate the quality of entire fibers or individual pixels within these frames, accounting for cases of broken and/or unplugged fibers, cosmic rays, sky-subtraction failures, etc. A catch-all summary bit 3DREJECT is set when a given pixel should be excluded from use in building a 3D composite data cube.

The MaNGA DRP 3D spaxel masks applicable to these composite data cubes are given in Table 14. Since these cubes combine across many individual exposures, the 3D spaxel masks are necessarily less detailed than the 2D pixel masks, and indicate simply the overall quality of individual spaxels within a given data cube. This includes whether there is no

Written by: https://svn.sdss.org/public/repo/manga/mangadrp/tags/v1_5_4/pro/spec3d/mdrp_reduceoneifu.pro

RSS Data Model: https://data.sdss.org/datamodel/files/MANGA_SPECTRO_REDUX/DRPVER/PLATE4/stack/manga-RSS.html

CubeData Model: https://data.sdss.org/datamodel/files/MANGA_SPECTRO_REDUX/DRPVER/PLATE4/stack/manga-CUBE.html

B.3. DRPall Summary Table

The 3D-stage reductions of the MaNGA DRP (including calibration mini-bundles) are summarized in the DRPall FITS file, drpall-[version].fits. This file aggregates metadata pulled from all individual reduced data cube files (plus spectrophotometric standard stars), as well as the NSA targeting catalog. Each row in this table corresponds to an individual observation. The DRPall summary file is a convenient place to quickly look for information regarding, for example, unique cube identifiers, achieved S/N, data quality, observing conditions, targeting bitmasks and basic NSA catalog parameters. The complete data model for the DRPall summary file can be found at https://data.sdss.org/datamodel/files/MANGA_SPECTRO_REDUX/DRPVER/drpall.html.

Table 15
MANGA_DRP2QUAL Data Quality Bits

Bit	Value	Label	Description
0	1	VALIDFILE	File is valid
1	2	EXTRACTBAD	Many bad values in extracted frame
2	4	EXTRACTBRIGHT	Extracted spectra abnormally bright
3	8	LOWEXPTIME	Exposure time less than 10 minutes
4	16	BADIFU	One or more IFUs missing/bad in this frame
5	32	HIGHSCAT	High scattered light levels
6	64	SCATFAIL	Failure to correct high scattered light levels
7	128	BADDITHER	Bad dither location information
8	256	ARCFOCUS	Bad focus on arc frames
9	512	RAMPAGINGBUNNY	Rampaging dust bunnies in IFU flats
10	1024	SKYSUBBAD	Bad sky subtraction
11	2048	SKYSUBFAIL	Failed sky subtraction
12	4096	FULLCLOUD	Completely cloudy exposure
13	8192	BADFLEXURE	Abnormally high flexure LSF correction

Table 16
MANGA_DRP3QUAL Data Quality Bits

Bit	Value	Label	Description
0	1	VALIDFILE	File is valid
1	2	BADDEPTH	IFU does not reach target depth
2	4	SKYSUBBAD	Bad sky subtraction in one or more frames
3	8	HIGHSCAT	High scattered light in one or more frames
4	16	BADASTROM	Bad astrometry in one or more frames
5	32	VARIABLELSF	LSF varies significantly between component spectra
6	64	BADOMEGA	Omega greater than threshold in one or more sets
7	128	BADSET	One or more sets are bad
8	256	BADFLUX	Bad flux calibration
9	512	BADPSF	PSF estimate may be bad
30	1,073,741,824	CRITICAL	Critical failure in one or more frames

coverage (i.e., outside the footprint of the IFU bundle), low coverage (near the edges of the IFU bundle), a dead fiber (which will in turn cause low and/or no coverage within the bundle), or a foreground star that should be masked for many science analyses. These foreground stars are identified manually using a combination of SDSS imaging and the MaNGA data cubes, and stored in a reference list read by the DRP. A catch-all DONOTUSE flag indicates a superset of all pixels that should not be used for science.

The progress of a given exposure through the DRP is controlled by use of the MANGA_DRP2QUAL maskbit (Table 15, which indicates any potential problems that affect the reduction of the exposure. These range from the informative for operations (RAMPAGINGBUNNY indicates dust accumulation on the IFU surfaces that must be cleaned) to the fatal (FULLCLOUD indicates that the transparency is too low to successfully flux calibrate the data).

The final quality of a given object processed by the 3D stage of the DRP is indicated by the reduction quality bit MANGA_DRP3QUAL (Table 16). This single integer refers to the quality of an entire galaxy data cube, and can indicate a variety of possible problems sorted roughly in increasing order of importance from low average depth (BADDEPTH) to a CRITICAL failure that means that the data should be treated with great caution or (conservatively) omitted from science analyses. We note that many of even the CRITICAL failure cases may represent an overly vigorous QA algorithm rather than any intrinsic problem in the data though; these routines will continue to be refined throughout SDSS-IV.

We note that additional bits may be added to each of these quality-control bitmasks over the lifetime of the survey. An online version can be found at <http://www.sdss.org/dr13/algorithms/bitmasks/> for DR13, and at similar locations for future data releases.

REFERENCES

- Abazajian, K., Adelman-McCarthy, J. K., Agüeros, M. A., et al. 2003, *AJ*, **126**, 2081
- Adams, J. J., Blanc, G. A., Hill, G. J., et al. 2011, *ApJS*, **192**, 5
- Allen, J. T., Croom, S. M., Konstantopoulos, I. S., et al. 2015, *MNRAS*, **446**, 1567
- Andersen, D. R., Bershady, M. A., Sparke, L. S., et al. 2006, *ApJS*, **166**, 505
- Bacon, R., Copin, Y., Monnet, G., et al. 2001, *MNRAS*, **326**, 23
- Belfiore, F., Maiolino, R., Bundy, K., et al. 2015, *MNRAS*, **449**, 867
- Bershady, M. A. 2009, arXiv:0910.0167
- Bershady, M. A., Martinsson, T. P. K., Verheijen, M. A. W., et al. 2011, *ApJL*, **739**, L47
- Bershady, M. A., Verheijen, M. A. W., Swaters, R. A., et al. 2010, *ApJ*, **716**, 198
- Birkmann, S. M., Ferruit, P., Alves de Oliveira, C., et al. 2014, *Proc. SPIE*, **9143**, 914308
- Blanc, G. A., Weinzirl, T., Song, M., et al. 2013, *AJ*, **145**, 138
- Blanton, M. R., Kazin, E., Muna, D., Weaver, B. A., & Price-Whelan, A. 2011, *AJ*, **142**, 31
- Blecha, A., Cayatte, V., North, P., Royer, F., & Simond, G. 2000, *Proc. SPIE*, **4008**, 467
- Bolton, A. S., & Burles, S. 2007, *NJPh*, **9**, 443
- Bolton, A. S., Schlegel, D. J., Aubourg, É., et al. 2012, *AJ*, **144**, 144
- Bundy, K., Bershady, M. A., Law, D. R., et al. 2015, *ApJ*, **798**, 7
- Cappellari, M., Emsellem, E., Krajnović, D., et al. 2011a, *MNRAS*, **413**, 813
- Cappellari, M., Emsellem, E., Krajnović, D., et al. 2011b, *MNRAS*, **416**, 1680
- Closs, M. F., Ferruit, P., Lobb, D. R., et al. 2008, *Proc. SPIE*, **7010**, 701011

- Colina, L., Arribas, S., & Borne, K. D. 1999, *ApJL*, 527, L13
- Croom, S. M., Lawrence, J. S., Bland-Hawthorn, J., et al. 2012, *MNRAS*, 421, 872
- Davies, R. I. 2007, *MNRAS*, 375, 1099
- Davies, R. I., Agudo Berbel, A., Wiezorek, E., et al. 2013, *A&A*, 558, A56
- Dawson, K. S., Kneib, J.-P., Percival, W. J., et al. 2016, *AJ*, 151, 44
- Dawson, K. S., Schlegel, D. J., Ahn, C. P., et al. 2013, *AJ*, 145, 10
- de Zeeuw, P. T., Bureau, M., Emsellem, E., et al. 2002, *MNRAS*, 329, 513
- Dekel, A., Sari, R., & Ceverino, D. 2009, *ApJ*, 703, 785
- Dopita, M., Rhee, J., Farage, C., et al. 2010, *Ap&SS*, 327, 245
- Drory, N., MacDonald, N., Bershad, M. A., et al. 2015, *AJ*, 149, 77
- Filippenko, A. V. 1982, *PASP*, 94, 715
- Förster Schreiber, N. M., Genzel, R., Bouché, N., et al. 2009, *ApJ*, 706, 1364
- Förster Schreiber, N. M., Genzel, R., Newman, S. F., et al. 2014, *ApJ*, 787, 38
- Förster Schreiber, N. M., Shapley, A. E., Genzel, R., et al. 2011, *ApJ*, 739, 45
- Fruchter, A. S., & Hook, R. N. 2002, *PASP*, 114, 144
- García-Benito, R., Zibetti, S., Sánchez, S. F., et al. 2015, *A&A*, 576, A135
- Greisen, E. W., Calabretta, M. R., Valdes, F. G., & Allen, S. L. 2006, *A&A*, 446, 747
- Gunn, J. E., Siegmund, W. A., Mannery, E. J., et al. 2006, *AJ*, 131, 2332
- Hopkins, A. M., Driver, S. P., Brough, S., et al. 2013, *MNRAS*, 430, 2047
- Horne, K. 1986, *PASP*, 98, 609
- Husemann, B., Jahnke, K., Sánchez, S. F., et al. 2013, *A&A*, 549, A87
- Kauffmann, G., Heckman, T. M., White, S. D. M., et al. 2003, *MNRAS*, 341, 33
- Krabbe, A., Gasaway, T., Song, I., et al. 2004, *Proc. SPIE*, 5492, 1403
- Law, D. R., Shapley, A. E., Steidel, C. C., et al. 2012, *Natur*, 487, 338
- Law, D. R., Steidel, C. C., Erb, D. K., et al. 2009, *ApJ*, 697, 2057
- Law, D. R., Yan, R., Bershad, M. A., et al. 2015, *AJ*, 150, 19
- Li, C., Wang, E., Lin, L., et al. 2015, *ApJ*, 804, 125
- Martinsson, T. P. K., Verheijen, M. A. W., Westfall, K. B., et al. 2013, *A&A*, 557, A130
- Massey, P., & Foltz, C. B. 2000, *PASP*, 112, 566
- Modigliani, A., Hummel, W., Abuter, R., et al. 2007, arXiv:astro-ph/0701297
- Moore, A. M., Larkin, J. E., Wright, S. A., et al. 2014, *Proc. SPIE*, 9147, 914724
- Newman, J. A., Cooper, M. C., Davis, M., et al. 2013, *ApJS*, 208, 5
- Noll, S., Kausch, W., Kimeswenger, S., et al. 2014, *A&A*, 567, A25
- Osterbrock, D. E., Fulbright, J. P., Martel, A. R., et al. 1996, *PASP*, 108, 277
- Rousselot, P., Lidman, C., Cuby, J.-G., Moreels, G., & Monnet, G. 2000, *A&A*, 354, 1134
- Sánchez, S. F. 2006, *AN*, 327, 850
- Sánchez, S. F., Kennicutt, R. C., Gil de Paz, A., et al. 2012, *A&A*, 538, A8
- Sandin, C., Becker, T., Roth, M. M., et al. 2010, *A&A*, 515, A35
- Schlegel, D. J., Finkbeiner, D. P., & Davis, M. 1998, *ApJ*, 500, 525
- Sharp, R., Allen, J. T., Fogarty, L. M. R., et al. 2015, *MNRAS*, 446, 1551
- Smee, S. A., Gunn, J. E., Uomoto, A., et al. 2013, *AJ*, 146, 32
- Snigula, J. M., Drory, N., Fabricius, M., et al. 2014, adass XXIII, 485, 447
- Thomas, D., Maraston, C., Schawinski, K., Sarzi, M., & Silk, J. 2010, *MNRAS*, 404, 1775
- Tremonti, C. A., Heckman, T. M., Kauffmann, G., et al. 2004, *ApJ*, 613, 898
- Walcher, C. J., Wisotzki, L., Bekeraité, S., et al. 2014, *A&A*, 569, A1
- Weilbacher, P. M., Streicher, O., Urrutia, T., et al. 2012, *Proc. SPIE*, 8451, 84510B
- Wells, M., Pel, J.-W., Glasse, A., et al. 2015, *PASP*, 127, 646
- Wilkinson, D. M., Maraston, C., Thomas, D., et al. 2015, *MNRAS*, 449, 328
- Wilson, J. C., Hearty, F., Skrutskie, M. F., et al. 2010, *Proc. SPIE*, 7735, 77351C
- Wing, R. F., & Ford, W. K., Jr. 1969, *PASP*, 81, 527
- Wisnioski, E., Förster Schreiber, N. M., Wuyts, S., et al. 2015, *ApJ*, 799, 209
- Wright, S. A., Larkin, J. E., Moore, A. M., et al. 2014, *Proc. SPIE*, 9147, 91479S
- Yan, R., Bundy, K., Law, D., et al. 2016b, *AJ*, in press, arXiv:1607.08613
- Yan, R., Tremonti, C., Bershad, M. A., et al. 2016a, *AJ*, 151, 8
- York, D. G., Adelman, J., Anderson, J. E., Jr., et al. 2000, *AJ*, 120, 1579
- Zanichelli, A., Garilli, B., Scodreggio, M., et al. 2005, *PASP*, 117, 1271